Nutritional iron deficiency elicits profound rewiring of red pulp macrophage functions via high FPN and SYK-mediated signaling

Pratik Kumar Mandal[1#], Komal Chouhan[1#], Patryk Slusarczyk[1#], Raghunandan Mahadeva[1#], Gabriela Zurawska[1], Marta Niklewicz[1], Aneta Jończy[1], Małgorzata Lenartowicz[2], Wojciech Pokrzywa[1], Delphine Meynard[3], Elizabeta Nemeth[4] and Katarzyna Mleczko-Sanecka[1#]

1 International Institute of Molecular and Cell Biology in Warsaw, Poland

2 Laboratory of Genetics and Evolution, Institute of Zoology and Biomedical Research, Jagiellonian University, Cracow, Poland

3 Institut de Recherche en Santé Digestive (IRSD), Université de Toulouse, INSERM, INRA, ENVT, Toulouse, France

4 David Geffen School of Medicine at UCLA, Los Angeles, California, United States.

# - equal contribution

To whom correspondence may be addressed: Katarzyna Mleczko-Sanecka, International Institute of Molecular and Cell Biology in Warsaw, 4 Ks. Trojdena Street, 02-109 Warsaw, Poland, E-mail: kmsanecka@iimcb.gov.pl

ABSTRACT

Iron deficiency is a globally prevalent nutritional disorder with significant socio-medical impacts, yet the mechanisms by which different cell types adapt to iron restriction remain poorly understood. Splenic red pulp macrophages (RPMs) manage the highest iron flux in the body by recycling aged red blood cells (RBCs) through erythrophagocytosis. In this study, we investigated the adaptive mechanisms employed by RPMs under systemic iron deficiency. We found that RPMs from mildly anemic, dietary iron-deficient (ID) mice exhibit a surprising enhancement in erythrophagocytic capacity, accompanied by elevated cytoplasmic labile iron levels, reduced iron stores, and increased iron-export capacity via ferroportin (FPN). Proteomic profiling, validated by flow cytometry, revealed increased mass and activity of both lysosomes and mitochondria in RPMs from ID mice, along with upregulated expression of apoptotic cell receptors. Further assays identified a marked increase in mitochondrial respiration in ID RPMs, a unique response that contrasts with prior reports of impaired mitochondrial function in iron-deficient cells. These responses occurred independently of classical M2 polarization markers. Using both *in vivo* and cellular models, we identified the low hepcidin–high FPN axis as a key driver of the phagocytic and metabolic rewiring in RPMs. Additionally, calcium signaling emerged as a likely mediator of this axis. Pharmacological inhibition of calcium signaling effectors pinpointed SYK kinase as a molecular switch governing the high-FPN-induced functional reprogramming of macrophages. Short-term SYK inhibition reduced the enhanced erythrophagocytic function of RPMs during iron deficiency, impairing iron utilization for extramedullary splenic erythropoiesis. Together, our findings highlight metabolic reprogramming in RPMs as a strategic adaptation that optimizes their iron recycling and utilization capacity in response to systemic iron scarcity.

INTRODUCTION

Efficient clearance of apoptotic cells, termed efferocytosis, is fundamental to tissue homeostasis and the prevention of inflammation by averting the release of potentially damaging intracellular components into the surrounding microenvironment[1–4]. Macrophages, the primary phagocytes responsible for efferocytosis, undergo profound metabolic reprogramming to sustain this process. Metabolite-driven receptor activation (e.g., PPARδ, LXR) promotes continual efferocytosis[5–7] coupled with enhanced glycolysis[8,9], fatty acid oxidation[10] mitochondrial respiration and dynamics[11,12], increased glutamine and arginine breakdown[13,14], and an upregulated pentose phosphate pathway[13,15,16]. However, a critical gap remains in our understanding of how diverse metabolic changes are integrated and regulated across macrophage subsets and specialized efferocytic processes. In particular, very little is known about the metabolic or signaling control of erythrophagocytosis (EP), the process of clearing physiologically aged or damaged red blood cells (RBCs), which is predominantly carried out by red pulp macrophages (RPMs) in the spleen[17,18]. As RBCs constitute the body's largest iron store, their efficient removal and subsequent iron recovery are critical for supporting erythropoiesis[18,19]. Upon engulfment, RBCs are processed within phagolysosomes, releasing heme, which is catabolized by heme oxygenase 1 (HO-1) into ferrous iron (Fe^{2+}) that feeds the cellular labile iron pool (LIP). Within RPMs, iron from the LIP is either stored within ferritin or exported via ferroportin (FPN) to replenish circulating transferrin-bound iron. The iron export capacity of FPN is tightly regulated by hepcidin, a liver-derived hormone that provokes occlusion and degradation of FPN, thus ensuring systemic iron homeostasis. The central role of RPMs in the maintenance of iron homeostasis is underscored by the functional attenuation in RBC clearance, accompanied by progressive splenic iron accumulation, observed in mice lacking genes essential for RPM development and during physiological aging[20–22]. Emerging evidence indicates that EP is regulated by diverse factors, including pro-inflammatory signals[23–25], calcium (Ca^{2+}) signaling[21,26], the mechanosensitive channel PIEZO1[26], and iron accumulation[21]. How these factors interact to fine-tune EP in response to varying physiological demands, particularly in states of altered iron bioavailability, remains a key unanswered question.

The critical nature of the RPM-driven recycling system takes on new significance when we consider the global burden of iron deficiency, the main cause of anemia, which impacts nearly 2 billion people (approximately 30% of the population)[27–30]. According to the 2021 Global Burden of Disease study, anemia is the third leading contributor to years lived with disability globally, and, despite its multifactorial etiology, dietary iron deficiency remains the predominant contributor worldwide[29,31]. Critically, the prevalence of iron deficiency itself significantly exceeds that of clinically diagnosed anemia and represents a crucial intersection between cellular iron metabolism and public health outcomes, particularly in resource-constrained developing regions[32–35]. Yet, the specific cellular vulnerabilities and the molecular mechanisms orchestrating adaptation to iron deficiency, especially within iron-recycling splenic RPMs, remain poorly defined.

Here, we demonstrate that RPMs in iron-deficient mice exhibit enhanced EP, and we explore how this functional adjustment is regulated by cellular signaling and metabolic rewiring. We reveal that the hepcidin-FPN axis, via regulating Ca^{2+} and SYK signaling enhances the EP capacity of RPMs together with the mitochondrial respiration to optimize iron recycling during iron deficiency. This highlights the metabolic and functional plasticity of RPMs during limited iron supplies.

RESULTS

Nutritional iron deficiency increases the EP capacity in RPMs

To investigate the impact of low systemic iron availability on EP and more broadly the iron-recycling capacity of RPMs, we employed a murine model of nutritional iron deficiency. To this end, four-week-old female mice were subjected to either an iron-deficient (ID) diet (<5 ppm iron) or an iron-balanced (IB) control diet (200 ppm iron) for five weeks. Dietary iron restriction resulted in significantly decreased splenic (Figure 1A) and hepatic (Figure 1B) non-heme iron concentrations in the ID group compared to the IB group, confirmed by reduced iron deposition within the splenic red pulp via Perl's staining (Figure S1A). A subtle but significant reduction in cardiac (Figure S1B) non-heme iron was also observed in the ID group, while muscle (Figure S1C) tissue iron content remained unaffected. These data suggested a tissue-specific response to dietary iron restriction, with the spleen and the liver, the organs for iron recycling and storage, being the most affected. Consistent with limited iron delivery, transferrin saturation (Figure 1C) was markedly reduced in ID mice, leading to mild microcytic hypochromic anemia (Figure 1D, S1D, and S1E), which hallmarks iron deficiency. Expectedly, ID mice displayed compensatory

58 mechanisms manifested by splenic stress erythropoiesis, as evidenced by elevated serum
59 erythropoietin (EPO) (Figure S1F) and increased percentage of splenic, but not bone marrow,
60 $CD71^+$/$Ter119^+$ progenitor cells (Figure 1E).

61 Next, we aimed to precisely characterize cell-intrinsic iron parameters of RPMs in response to iron-
62 restricted feeding. Consistent with the drop in serum levels of the iron-regulatory hormone hepcidin
63 (Figure 1F), FPN expression in RPMs, assessed by immunofluorescence and flow cytometry
64 (Figure 1G and 1H), was significantly elevated in ID mice. In agreement with boosted iron-export
65 capacity, a marked decrease in total iron content was observed in the magnetically sorted RPMs of
66 ID mice (Figure 1I), along with reduced protein expression of both L- and H-ferritin (FTL and
67 FTH1) (Figure 1J and 1K), indicating depletion of intracellular iron stores. Furthermore, we
68 detected upregulated levels of transferrin receptor 1 (TFR1) surface expression (Figure 1L),
69 implying a cellular response to iron deficiency. However, paradoxically, despite enhanced iron
70 export, RPMs in ID mice unexpectedly displayed a mild but significant elevation of LIP, as
71 assessed using the Fe^{2+}-specific fluorescent probe FerroOrange (Figure 1M). Consistent with this
72 finding, we also detected elevated reactive oxygen species (ROS) levels in RPMs of ID versus IB
73 mice (Figure 1N).

74 Intrigued by the increased LIP in RPMs of ID mice, we investigated the capacity of EP, the major
75 route for RPM iron acquisition. To this end, we transfused mice with PKH67-labeled RBCs.
76 Strikingly, flow cytometry analysis revealed significantly enhanced phagocytosis of temperature-
77 stressed RBCs (sRBC) by RPMs from ID compared to IB mice, a phenomenon not observed for
78 non-stressed fresh RBCs that were engulfed at comparably low levels (Figure 1O). In addition, we
79 evaluated EP capacity across other myeloid populations, including Kupffer cells (KCs) in the liver,
80 macrophages in the bone marrow, and circulating monocytes (Figure 1O). Among these, only KCs
81 showed a statistically significant, albeit modest, increase in EP capacity in iron-restricted mice.
82 Previous work has shown that splenic red pulp sinuses trap aged RBCs, leading to partial hemolysis
83 and subsequent phagocytosis of membrane remnants (RBC ghosts) by RPMs[36]. To distinguish
84 between the clearance of intact sRBCs and RBC ghosts in our model, we intravenously injected
85 mice with sRBCs ubiquitously expressing GFP and stained them with PKH26 membrane dye.
86 Consistent with our prior results, RPMs from ID mice exhibited increased EP of GFP^+ $PKH26^+$
87 sRBCs compared to control IB animals, confirming their enhanced capability for the uptake of

88 intact RBCs (Figure 1P). Likewise, splenic clearance of transfused GFP sRBCs was accelerated in
89 ID mice compared to IB controls (Figure 1Q), further supporting enhanced sRBC removal by
90 RPMs within the splenic microenvironment. To validate sRBC transfusion assay results, we next
91 assessed intracellular levels of the erythrocyte marker TER-119 in RPMs as a measure of
92 endogenous EP capacity[21,37], confirming its elevation in ID mice (Figure 1R). Finally, we verified
93 whether increased EP in low iron mice is solely driven by macrophage-intrinsic mechanisms or
94 could result from erythrocyte-derived signals. RBC lifespan remained comparable between IB and
95 ID mice (Figure 1S), suggesting that iron restriction did not compromise RBC integrity. Next,
96 exposure of the apoptotic cell marker phosphatidylserine in splenic RBCs was not enhanced in ID
97 compared to IB mice (Figure 1T). Finally, using a co-culture assay of magnetically isolated splenic
98 and circulating RBCs with primary macrophages, we found that while aged splenic RBCs are
99 preferentially sequestered compared to circulating RBCs (Figure 1U), iron deficiency does not
100 increase splenic RBC susceptibility to phagocytosis (Figure 1V), implying no induction of RBC
101 "eat-me" signals by iron restriction. Taken together, we uncovered that systemic iron restriction
102 potentiates the cell-intrinsic RBC clearance capacity of RPMs, likely aimed at balancing the
103 increased replenishment of TF-bound iron pool by FPN-mediated export.

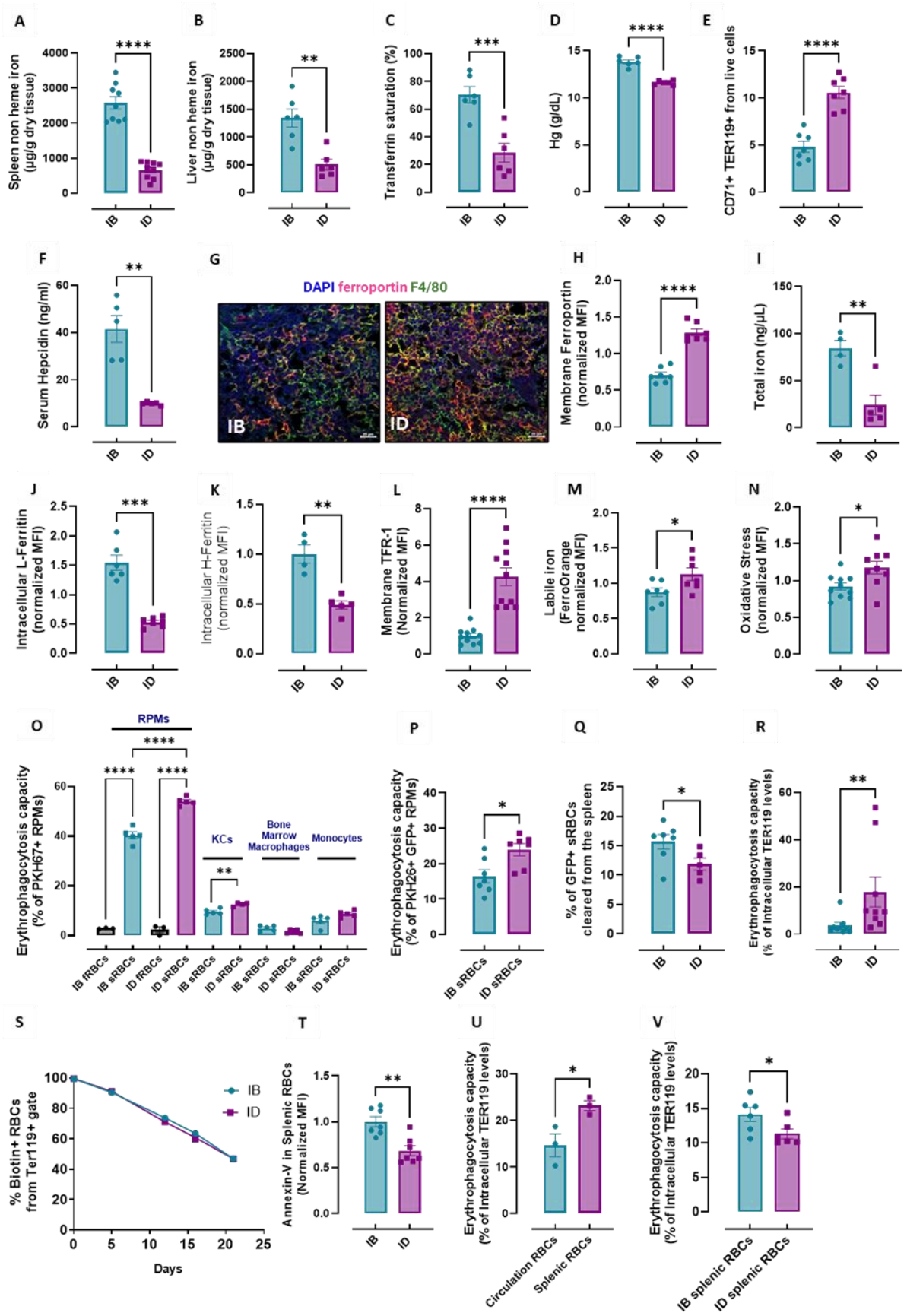
A
Spleen non heme iron (µg/g dry tissue)
B
Liver non heme iron (µg/g dry tissue)
C
Transferrin saturation (%)
D
Hg (g/dL)
E
CD71+ TER119+ from live cells
F
Serum Hepcidin (ng/ml)
G
DAPI ferroportin F4/80
IB
ID
H
Membrane Ferroportin (normalized MFI)
I
Total iron (ng/µL)
J
Intracellular L-Ferritin (normalized MFI)
K
Intracellular H-Ferritin (normalized MFI)
L
Membrane TFR-1 (Normalized MFI)
M
Labile iron (FerroOrange normalized MFI)
N
Oxidative Stress (normalized MFI)
O
RPMs
KCs
Bone Marrow Macrophages
Monocytes
Erythrophagocytosis capacity (% of PKH67+ RPMs)
IB fRBCs
IB sRBCs
ID fRBCs
ID sRBCs
P
Erythrophagocytosis capacity (% of PKH26+ GFP+ RPMs)
Q
% of GFP+ sRBCs cleared from the spleen
R
Erythrophagocytosis capacity (% of Intracellular TER119 levels)
S
% Biotin+ RBCs from Ter119+ gate
Days
T
Annexin-V in Splenic RBCs (Normalized MFI)
U
Circulation RBCs
Splenic RBCs
V
IB splenic RBCs
ID splenic RBCs

104

Figure 1. Nutritional iron deficiency increases the EP capacity in RPMs

(A) Spleen and (B) liver non-heme iron content was determined in IB and ID mice. (C) Plasma transferrin saturation was determined in IB and ID mice. (D) Blood hemoglobin (Hg) was determined in IB and ID mice. (E) Shown is the percentage of erythroid progenitor cells (TER119+ CD71+) present in the spleen of IB and ID mice. (F) Serum hepcidin levels were measured in IB and ID mice with the Hepcidin-Murine Compete ELISA Kit. (G) Representative confocal microscopy images of FPN stabilization in the splenic red pulp of IB and ID mice. (H) Expression of ferroportin on the cell membrane of RPMs derived from IB and ID mice was assessed by flow cytometry. (I) The total intracellular iron content in magnetically sorted RPMs from IB and ID mice was assessed using the Iron Assay Kit. (J) Intracellular L-ferritin and (K) H-ferritin protein levels in RPMs of IB and ID mice were quantified by flow cytometry. (L) Expression of TFR1 on the cell membrane of RPMs derived from IB and ID mice was assessed by flow cytometry. (M) Cytosolic ferrous iron (Fe^{2+}) levels in RPMs of IB and ID mice were measured using FerroOrange with flow cytometry. (N) The cytosolic ROS levels in RPMs of IB and ID mice were assessed by determining CellROX Deep Red fluorescence intensity with flow cytometry. (O) The erythrophagocytosis (EP) capacity in RPMs and other myeloid populations of IB and ID mice was determined using flow cytometry by measuring the percentage of cells that phagocytosed transfused PKH67-labeled RBCs. fRBCs indicate fresh RBCs, sRBCs - stressed RBCs (shown only for RPMs, in other indicated populations fRBCs uptake was also substantially lower than sRBCs). (P) IB and ID mice were transfused with GFP-expressing sRBCs and stained with a membrane dye PKH26. The percentage of RPMs positive for intact RBCs ($PKH26^{+}GFP^{+}$) was determined. (Q) Flow cytometric analysis of splenic GFP-sRBC clearance in ID vs IB mice. (R) The endogenous EP capacity of RPMs derived from IB and ID mice was determined by intracellular staining of the RBC marker TER119 in RPMs and flow cytometry. (S) The RBC biotinylation lifespan assay was performed on circulating RBCs from IB and ID mice. (T) Flow cytometry assessment of phosphatidylserine exposure (Annexin V staining) in splenic RBCs, comparing ID vs IB mice, as markers of natural RBC aging. (U) Comparison of EP capacity between splenic and circulating RBCs of IB mice. (V) EP capacity of iRPMs exposed to RBCs derived from the spleens of IB and ID mice. Each dot represents one mouse or an independent cell-based experiment. Each dot in the graph (S) represents n=9. Data are represented as mean ± SEM. Welch's unpaired t-test determined statistical significance between the two groups. ns $p>0.05$, *$p<0.05$, **$p<0.01$, ***$p<0.001$ and ****$p<0.0001$.

Iron deficiency drives metabolic reprogramming and enhanced lysosomal activity of RPMs via the non-classical type of polarization

To decipher the molecular mechanisms of enhanced EP capacity in RPMs of ID mice and explore potential accompanying functional changes, we first investigated the transcriptome of FACS-isolated RPMs. Surprisingly, only 145 genes were differentially expressed between RPMs derived from ID and IB mice (Figure 2A). Bioinformatic analysis revealed significant enrichment of cell cycle regulators (e.g., *Mki67, Plk1, Plk2, Aurka, E2f7, Sgo1, Kif4, Cenpf, Bub1, Ccnb1, Ccnb2*) among genes upregulated by iron deficiency. This suggested increased pro-mitotic signaling in RPM of ID mice, which was confirmed by elevated protein levels of the proliferation marker Ki67 (Figure 2B). However, using the Ms4a3Cre-RosaTdT reporter mice[38], we found no significant changes in the representation of embryonically-derived RPMs within the $CD45^{+}$ splenic population (Figure 2C). Interestingly, the percentage of monocyte-derived RPMs likewise remained constant

146 at approximately 20% in both IB and ID mice (Figure 2C), implying that the EP enhancement was
147 not underlain by de novo monocyte recruitment.

148 To further explore the adaptation of RPMs to systemic iron deficiency, we employed TMT-based
149 quantitative proteomics of magnetically sorted F4/80-high RPMs. This analysis identified 420
150 proteins significantly more abundant and 282 decreased in RPMs of ID mice compared to IB mice
151 (Figure 2D). Confirming the quality of the proteomics analysis, we found FTH1 and FTL as top
152 downregulated hits, and TFR1 as the most induced protein in RPMs of iron-restricted mice.
153 Consistent with this expression pattern, IRP2, a regulator of cellular iron balance, was stabilized in
154 RPMs of ID mice. In agreement with RNA-seq data, we also detected an increase in several
155 regulators of cell cycle progression, such as AURKA, AURKB, PLK1, or CDK1 in RPMs of low-
156 iron mice. In contrast, proteomic analysis revealed a pronounced functional rewiring of RPMs in
157 ID mice, highlighting significant post-transcriptional regulation, with far more protein-level
158 alterations and minimal overlap between transcriptomic and proteomic datasets. (Figure 2E). First,
159 we observed upregulation of the phosphatidylserine-recognizing phagocytic receptors MERTK
160 (Figure 2G) and TIM4 (significant hits) (Figure S2.1A), and a trend towards induction of AXL
161 (Figure 2H) and STAB2 (Figure S2.1B), along with the Fc receptor CD16 in RPMs of ID mice
162 (Figure S2.1C), responses that were all confirmed by flow cytometry. Interestingly, these increased
163 "eat me" signals were accompanied by the induction of the "don't eat me" receptor SIRPα on RPMs
164 in ID mice (Figure S2.1D), hinting at a mechanism that promotes the clearance of aged
165 dysfunctional RBCs sparing those that are intact. Next, to gain unbiased insights into processes
166 supporting the enhanced EP capacity of RPMs in ID mice, we performed functional enrichment
167 analyses on the differentially expressed proteins. Notably, mitochondrial proteins emerged as the
168 most significantly enriched category among hits upregulated in RPMs of ID compared to IB mice
169 (Figure 2F), including factors involved in ATP synthesis (ATP5S), metabolite transport (SLC25A5,
170 VDAC1), mitochondrial protein import (SAMM50), iron-sulfur cluster assembly (SFXN2), cristae
171 remodeling (MCCC1, PMPCB), and coenzyme Q-10 biosynthesis (COQ9, COQ5). Flow
172 cytometric analysis confirmed these expanded mitochondrial functions by demonstrating a
173 significant increase in both mitochondrial membrane potential (a measure of mitochondrial
174 activity) (Figure 2I) and mitochondrial mass (Figure 2J) in RPMs of ID mice. Consistently, RPMs
175 of ID versus IB mice exhibited increased uptake of fluorescently labeled glucose analog (Figure
176 2K) and showed a significant upregulation of protein synthesis (Figure 2L), a major ATP-

177 consuming process reflective of enhanced cellular bioenergetics. Interestingly, ATP levels in
178 FACS-sorted RPMs revealed a mild depletion in ID compared to IB mice (Figure 2M), but the
179 activation status of AMPK, a key sensor of cellular energy stress, was not enhanced (Figure 2N).
180 This suggests that RPMs of ID mice did not exhibit energy deficit, but rather a state where increased
181 ATP production is insufficient to meet the high ATP demand driven by accelerated EP and protein
182 synthesis. Importantly, in contrast to RPMs, neither iron-recycling KCs nor peritoneal
183 macrophages, which are not involved in iron recycling, show hallmarks of metabolic rewiring in
184 ID mice, as exemplified by unaltered mitochondrial activity and mass (Figure S2.1E-H).

185 Further analysis of the proteomic data revealed another major category, encompassing proteins
186 associated with lysosomal functions, as enriched in RPMs of ID compared to IB mice (Figure 2F).
187 In total, RPMs of iron-restricted mice increased the protein levels of 25 key components of the
188 Coordinated Lysosomal Expression and Regulation (CLEAR) network, a transcriptional program,
189 that drives lysosomal biogenesis and function[39]. This included integral lysosomal membrane
190 proteins, LAMP1 and LAMP2, vacuolar ATPase subunits (ATP6V0D1, ATP6V0A1), essential for
191 lysosomal acidification, and a diverse array of lysosomal hydrolases, including cathepsins B, D,
192 and S; α-glucosidase (GAA); β-glucosidase (GBA); N-acetylglucosaminidase (NAGA); and
193 sialidase 1 (NEU1). Flow cytometric analysis confirmed elevated intracellular LAMP1 levels
194 (Figure 2O), indicating increased lysosomal mass in RPMs of ID mice. Consistent with this, we
195 observed enhanced lysosomal activity in RPMs of ID mice using a fluorescent probe (Figure 2P).
196 Further ultrastructural analysis of RPMs within splenic sections with TEM revealed that while the
197 number of regular lysosomes, autophagolysomes, autophagosomes, and peroxisomes remained
198 unaltered between control and low-iron mice, large lysosomes were more abundant in RPMs of
199 iron-restricted mice (Figure S2.2B and S2.2C). While lysosomal size is dynamic and influenced by
200 nutrient availability, emerging evidence for instance from senescent cells suggests that a higher
201 proportion of enlarged lysosomes correlates with increased proteolytic activity and lysosomal
202 mass[40,41], remaining consistent with our observations. Taken together, these data suggest that
203 enhanced lysosomal function in RPMs of ID mice promotes heightened RBC degradation and
204 clearance, extending the spectrum of RPMs reprogramming in iron deficiency.

205 Erythrocytic heme and iron loading, as well as systemic or cell-intrinsic iron deficiency, have been
206 shown to influence macrophage polarization, promoting either pro-inflammatory or anti-

207 inflammatory profiles, though findings have often been contradictory[42–45]. Since metabolic
208 reprogramming is closely linked to macrophage polarization, which in turn shapes the outcome of
209 infections and inflammatory diseases[46], we assessed the polarization state of RPMs from iron-
210 restricted mice. Our RNA-seq and proteomics data revealed no clear induction of either pro- or
211 anti-inflammatory mediators, alongside a mixed expression pattern of surface signals identified by
212 flow cytometry. While some markers typically associated with M1 (MHCII, CD74) and M2
213 (CD206) polarization were decreased, others, such as the pro-inflammatory CD38 and the anti-
214 inflammatory CD163, were increased (Figure S2.3). This atypical combination of features suggests
215 that augmented RBC clearance in nutritionally iron-restricted mice leads to the activation state of
216 RPMs distinct from the M1 or M2 type of profile.

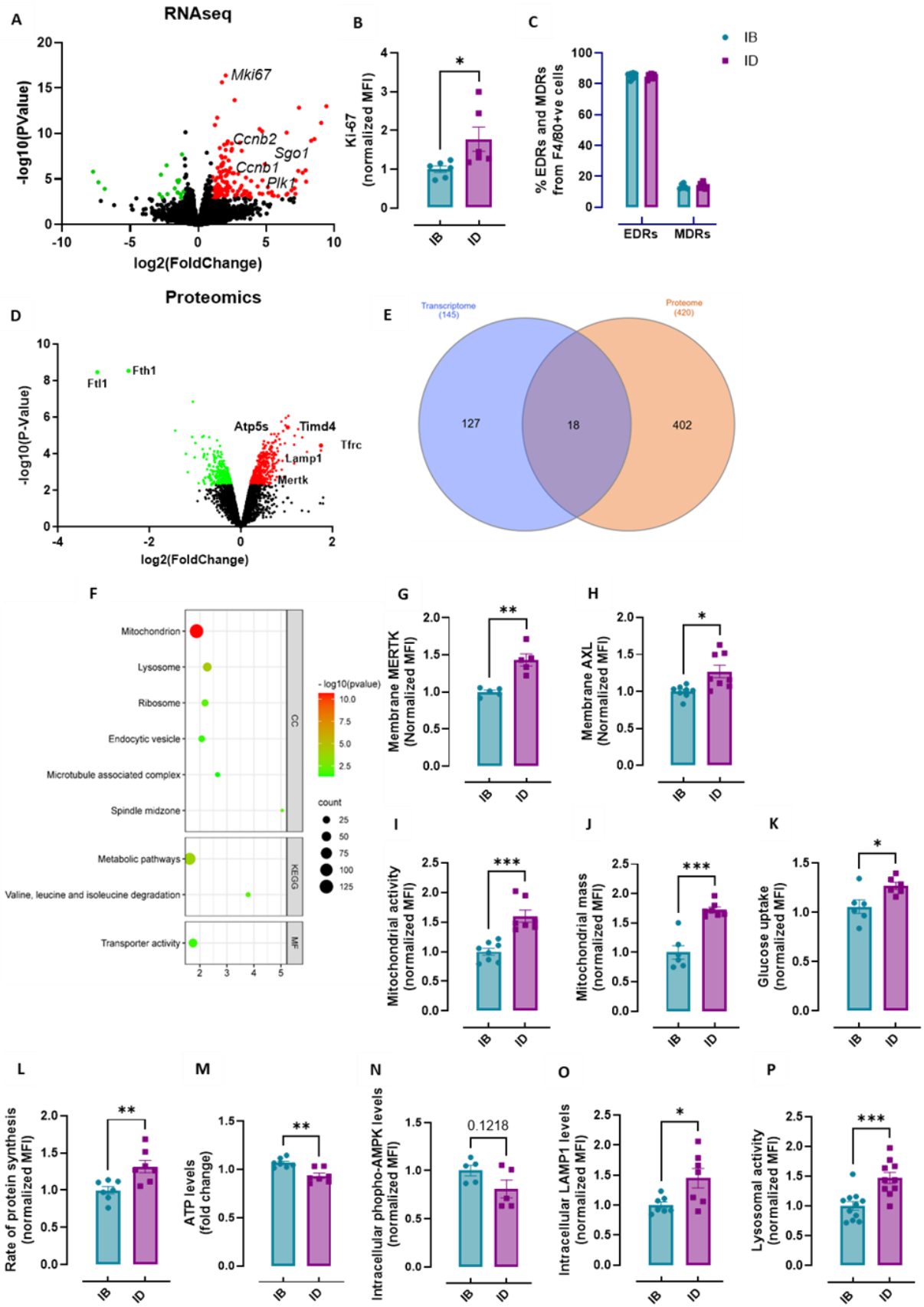
A
RNAseq
-log10(PValue)
log2(FoldChange)
Mki67
Ccnb2
Sgo1
Ccnb1
Plk1
B
Ki-67 (normalized MFI)
IB
ID
C
% EDRs and MDRs from F4/80+ve cells
EDRs
MDRs
IB
ID
D
Proteomics
-log10(P-Value)
log2(FoldChange)
Ftl1
Fth1
Atp5s
Timd4
Tfrc
Lamp1
Mertk
E
Transcriptome (145)
Proteome (420)
127
18
402
F
Mitochondrion
Lysosome
Ribosome
Endocytic vesicle
Microtubule associated complex
Spindle midzone
Metabolic pathways
Valine, leucine and isoleucine degradation
Transporter activity
CC
KEGG
MF
- log10(pvalue)
count
G
Membrane MERTK (Normalized MFI)
H
Membrane AXL (Normalized MFI)
I
Mitochondrial activity (normalized MFI)
J
Mitochondrial mass (normalized MFI)
K
Glucose uptake (normalized MFI)
L
Rate of protein synthesis (normalized MFI)
M
ATP levels (fold change)
N
Intracellular phopho-AMPK levels (normalized MFI)
0.1218
O
Intracellular LAMP1 levels (normalized MFI)
P
Lysosomal activity (normalized MFI)

217

Figure 2. **Iron deficiency drives metabolic reprogramming and enhanced lysosomal activity of RPMs**

(A) A volcano plot of differentially regulated genes identified by the RNASeq transcriptomic analysis in FACS-sorted RPMs derived from IB and ID mice. (B) Intracellular Ki-67 protein levels in RPMs derived from IB and ID mice were assessed by flow cytometry. (C) Percentage of embryonic-derived RPMs (EDRs) and monocyte-derived RPMs (MDRs) among F4/80^{+} cells in IB and ID mice. (D) Volcano plot visualizing the proteomic landscape of RPMs in response to iron deficiency, depicting differentially expressed proteins in IB and ID mice. (E) Venn diagram comparing the differentially expressed genes (transcriptome) and proteins (proteome) in RPMs from ID mice. (F) Enriched functional categories among proteins differentially expressed in magnetically sorted RPMs derived from ID versus IB spleen. Cell membrane expression levels of (G) MERTK and (H) AXL of RPMs in IB and ID mice were determined by using fluorescently labeled antibodies and flow cytometry. (I) Mitochondrial activity and (J) mitochondrial mass were determined in RPMs derived from IB and ID mice using TMRE probes and MitoTracker Green, respectively, with flow cytometry. (K) Quantification of glucose uptake via flow cytometry in RPMs from IB and ID mice using a fluorescent glucose analog. (L) Flow cytometric detection of newly synthesized proteins in RPMs of IB and ID mice using Click-iT Plus OPP Alexa Fluor 488 Protein Synthesis Assay. (M) Quantification of ATP levels in FACS-sorted RPMs (10,000 cells) from IB and ID mice using a chemiluminescence-based assay. (N) Intracellular phosphorylated AMPK protein levels in RPMs derived from IB and ID mice were assessed by flow cytometry. (O) Intracellular expression levels of the core lysosomal protein LAMP1 in RPMs of IB and ID mice were determined by flow cytometry. (P) Flow cytometric assessment of lysosomal activity in RPMs of IB and ID mice using the Lysosomal Intracellular Activity Assay Kit. Each dot represents one mouse. Data are represented as mean ± SEM. Welch's unpaired t-test determined statistical significance between the two groups. ns $p>0.05$, *$p<0.05$, **$p<0.01$, ***$p<0.001$ and ****$p<0.0001$.

The hepcidin-ferroportin axis regulates functional adaptations of RPMs during iron deficiency

To elucidate the mechanisms driving the enhanced EP capacity of RPMs in iron deficiency, we first investigated whether these adaptations were directly dependent on intracellular iron levels. Iron depletion in vitro using deferiprone (Figure 3A) or DFO[21] did not alter the RBC clearance capacity of primary BMDM macrophages cultured with hemine (iRPM). Furthermore, our *in vivo* data demonstrated that despite systemic iron deficiency, RPMs in ID mice exhibited elevated LIP (Figure 1M), likely due to their increased EP activity, indicating that iron chelation *in vitro* might not fully recapitulate the complex cellular interactions and signaling pathways present in RPMs *in vivo*. These findings suggested that factors beyond simple iron availability may be critical drivers of enhanced RPM phagocytic activity during iron deficiency. To address this possibility mechanistically, we developed an *in vitro* system using iRPMs cultured in serum derived from IB and ID mice, instead of bovine serum. This system recapitulated increased FPN and TFR1 expression in iRPMs exposed to ID serum, without a significant change in total iron levels (Figure 3B-D). Notably, cells cultured in ID serum exhibited enhanced EP (Figure S3A), suggesting that serum-borne factor is sufficient to rewire the phagocytic capacity of iRPMs towards RBCs. We first excluded the contribution of EPO, the cytokine previously implicated as a stimulator of

257 efferocytosis[47] . We showed that iRPMs, in contrast to BMDMs cultured without hemin which is
258 critical to mimic the heme and iron-rich nature of RPMs, did not enhance EP even under high EPO
259 doses (Figure S3B-C). Moreover, PPARγ, a factor proposed to act downstream of EPO[47] failed to
260 alter the EP capacity of iRPMs (Figure S3C). Next, inspired by a study that revealed low hepcidin,
261 rather than iron deficiency itself, as a key driver of pro-inflammatory responses in iron-restricted
262 mice[45], we proposed that reduced serum hepcidin levels and enhanced FPN stabilization in RPMs
263 might play a critical role in the adaptive reprogramming of these cells. Strikingly, a 4-hour
264 treatment with the hepcidin mimetic PR73 reversed the enhanced EP phenotype in iRPMs exposed
265 to ID, but to IB serum (Figure 3E and S3D). Likewise, we conducted live imaging of EP execution
266 by iRPMs incubated with serum from IB and ID mice, and exposed to RBCs labeled with dedicated
267 pHrodo™ dye that remains non-fluorescent at neutral pH but emits fluorescence in acidic
268 environments, such as in the phagolysosome. In line with our earlier flow cytometry results, we
269 observed the enhanced EP capacity of iRPMs treated with ID serum in real time (Figure 3F). This
270 boosted RBC clearance capacity was significantly abrogated upon 4 hours of PR73 treatment
271 (Figure 3F). Consistent with our *in vivo* observations, ID serum induced also a significant increase
272 in both mitochondrial and lysosomal activity, which was likewise abrogated by PR73 treatment
273 (Figure S3E-H).

274 To follow these *in vitro* observations, we next administered IB and ID mice with PR73 via
275 intraperitoneal injection four hours before analysis. PR73 administration effectively reduced cell-
276 surface FPN expression and induced hypoferremia in both dietary groups (Figure 3G-H). However,
277 total RPM iron content remained unchanged in both IB and ID mice following PR73 treatment
278 (Figure 3I). PR73 administration did not reverse the increased cell surface expression of TFR1 on
279 RPMs of ID mice but instead led to its further elevation, in contrast to IB mice where TFR1 levels
280 remained unaltered (Figure 3J). Interestingly, PR73 elicited likewise distinct effects on the LIP in
281 RPMs depending on the dietary regimen: it increased LIP levels in IB mice but led to a mild
282 decrease in ID mice (Figure 3K). The latter pattern was, interestingly, closely reflected by the
283 pronounced reversal of the elevated EP capacity of RPMs from ID mice (Figure 3L). Likewise,
284 PR73 abrogated most of the other hallmarks of RPM adaptation to iron deficiency, including
285 elevated mitochondrial activity, increased glucose uptake, and heightened protein synthesis (Figure
286 3M-O). Intriguingly, these modulating effects of PR73 were absent in IB mice. Furthermore, *ex*
287 *vivo* freshly isolated RPMs exhibited substantially elevated mitochondrial respiration, as assessed

288 by oxygen consumption rate measurement with Seahorse (Figure 3P). Strikingly, a 4-hour
289 preincubation of the RPMs of ID mice with PR73 completely abolished their activated oxygen
290 consumption (Figure 3P). Of note, these rapid effects of PR73 did not include changes in the
291 mitochondrial mass of RPMs (Figure S3I). Contrary to the abovementioned rewiring patterns,
292 lysosomal activity of RPMs of ID mice remained higher than in IB mice despite PR73
293 supplementation, suggesting distinct regulatory mechanisms governing this process (Figure S3J).
294 To support the key role of the hepcidin-FPN axis in modulating the iron-recycling activity of RPMs,
295 we employed *Tmprss6* knockout (KO) mice, a model of iron-refractory iron deficiency anemia
296 (IRIDA)[48–50]. This model exhibits characteristics similar to the nutritional ID model, including
297 reduced transferrin saturation, decreased hepatic and splenic iron stores (Figure S3K-M), and
298 anemia[49]. However, in contrast to dietary ID, *Tmprss6* KO mice display elevated hepcidin levels[51].
299 Importantly, we observed no significant difference in RPM's EP capacity between *Tmprss6* KO
300 mice and wild-type controls (Figure 3Q). Likewise, *in vitro* cultured iRPMs showed no difference
301 in RBC clearance when exposed to serum from either *Tmprss6* KO or wild-type mice (Figure 3R).
302 In, sum, these data implied that deficient hepcidin and FPN stabilization, hallmarks of nutritional
303 ID, are key driving factors for RPM functional and metabolic changes.

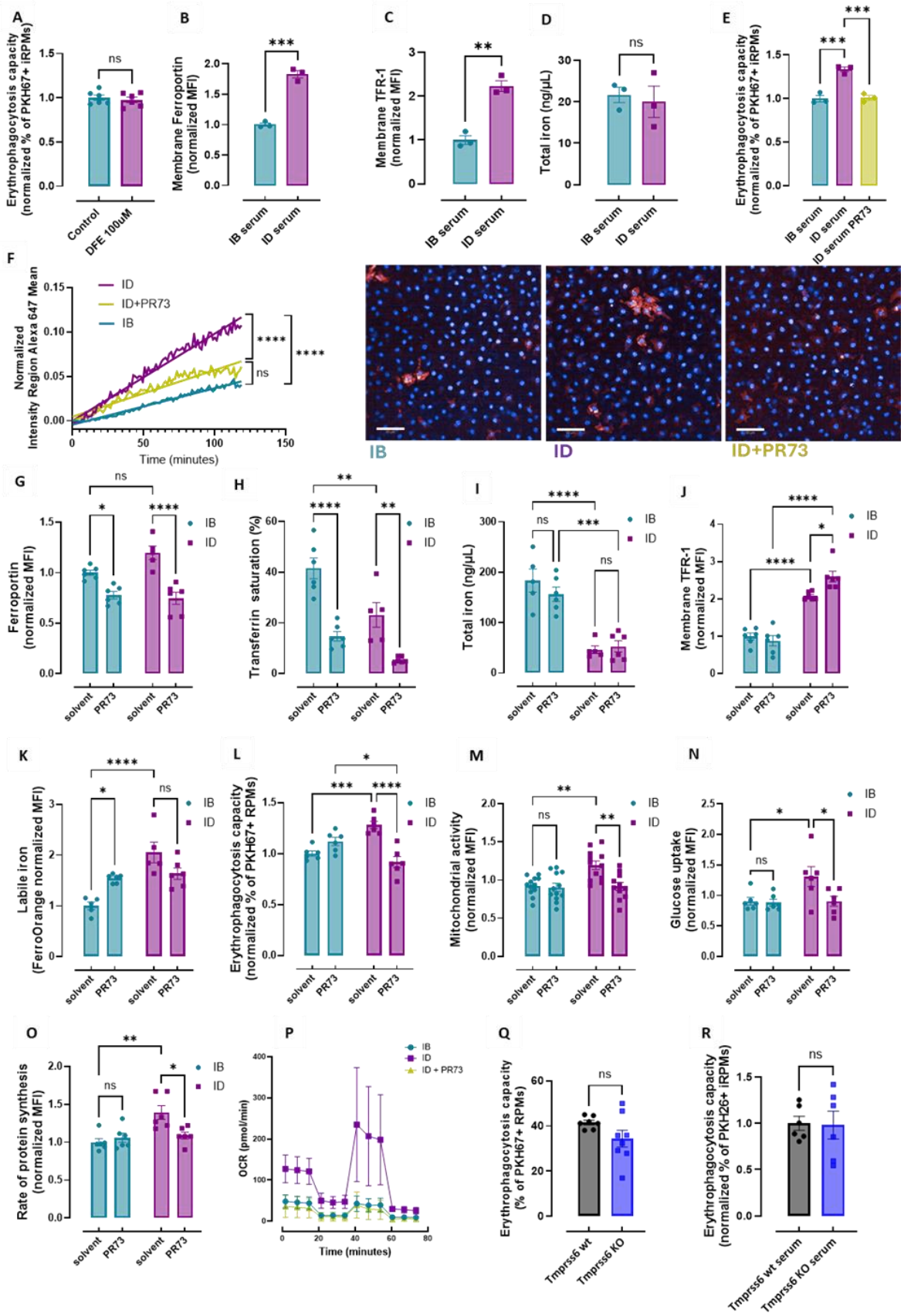
A
Erythrophagocytosis capacity (normalized % of PKH67+ iRPMs)
ns
Control
DFE 100uM
B
Membrane Ferroportin (normalized MFI)
***
IB serum
ID serum
C
Membrane TFR-1 (normalized MFI)
**
IB serum
ID serum
D
Total iron (ng/µL)
ns
IB serum
ID serum
E
Erythrophagocytosis capacity (normalized % of PKH67+ iRPMs)
***
***
IB serum
ID serum
ID serum PR73
F
Normalized Intensity Region Alexa 647 Mean
ID
ID+PR73
IB
****
****
ns
Time (minutes)
IB
ID
ID+PR73
G
Ferroportin (normalized MFI)
ns
*
****
IB
ID
solvent
PR73
solvent
PR73
H
Transferrin saturation (%)
**
****
**
IB
ID
solvent
PR73
solvent
PR73
I
Total iron (ng/µL)
****
ns
***
ns
IB
ID
solvent
PR73
solvent
PR73
J
Membrane TFR-1 (normalized MFI)
****
****
*
IB
ID
solvent
PR73
solvent
PR73
K
Labile iron (FerroOrange normalized MFI)
****
*
ns
IB
ID
solvent
PR73
solvent
PR73
L
Erythrophagocytosis capacity (normalized % of PKH67+ RPMs)
*
***
****
IB
ID
solvent
PR73
solvent
PR73
M
Mitochondrial activity (normalized MFI)
**
ns
**
IB
ID
solvent
PR73
solvent
PR73
N
Glucose uptake (normalized MFI)
*
*
ns
IB
ID
solvent
PR73
solvent
PR73
O
Rate of protein synthesis (normalized MFI)
**
ns
*
IB
ID
solvent
PR73
solvent
PR73
P
OCR (pmol/min)
IB
ID
ID + PR73
Time (minutes)
Q
Erythrophagocytosis capacity (% of PKH67+ RPMs)
ns
Tmprss6 wt
Tmprss6 KO
R
Erythrophagocytosis capacity (normalized % of PKH26+ iRPMs)
ns
Tmprss6 wt serum
Tmprss6 KO serum

304

Figure 3. **The hepcidin-ferroportin axis regulates functional adaptations of RPMs during iron deficiency**

(A) Normalized EP capacity of PKH67 sRBCs by cultured iRPMs treated with an iron chelator DFE (100 μM, 18 hr). (B) Flow cytometry analysis of surface ferroportin expression on iRPMs treated with serum from IB or ID mice. (C) Expression of TFR1 on the cell membrane of iRPMs treated with serum from IB or ID mice. (D) The total intracellular iron content in iRPMs treated with serum from IB or ID mice was assessed using the Iron Assay Kit. (E) The EP capacity in iRPMs treated with serum from IB or ID mice and serum from ID mice treated with the hepcidin agonist PR73 (50 nmol/mouse, 4 h) determined using flow cytometry by measuring the percentage of cells that phagocytosed transfused PKH26-labeled RBCs. (F) Time-lapse imaging of the execution of EP by iRPMs, exposed to pHrodo-stained sRBCs and cultured with the serum from IB and ID mice (with and without 4-h pretreatment with PR73). The left panel shows the quantification of the RBC fluorescent signal over time, normalized to the number of macrophages, over time. The right panel shows example images at the endpoint of the assay. Scale bar=50 mm. (G) Flow cytometric analysis of ferroportin cell surface expression on RPMs from IB and ID mice following intraperitoneal administration of the hepcidin agonist PR73 (50 nmol/mouse, 4 hours). (H) Plasma transferrin saturation was determined in IB and ID mice following PR73 administration. (I) Intracellular iron content in magnetically sorted RPMs from IB and ID mice post-PR73 treatment as determined using the Iron Assay Kit. (J) Flow cytometric evaluation of transferrin receptor 1 (TFR1) surface expression on RPMs derived from IB and ID mice post-PR73 administration. (K) Flow cytometric measurement of cytosolic ferrous iron (Fe^{2+}) levels in RPMs from IB and ID mice using FerroOrange following PR73 administration. (L) Normalized EP capacity of PKH67-sRBCs by RPMs from IB and ID mice after PR73 administration. (M) Mitochondrial activity was determined in RPMs derived from IB and ID mice using TMRE probe post-PR73 administration, with flow cytometry. (N) Quantification of glucose uptake via flow cytometry in RPMs from IB and ID mice upon PR73 administration using a fluorescent glucose analog. (O) Flow cytometric detection of newly synthesized proteins in RPMs of IB and ID mice using Click-iT Plus OPP Alexa Fluor 488 Protein Synthesis Assay after PR73 administration. (P) Seahorse analysis of ex-vivo RPMs from IB and ID mice, with or without 4-hour PR73 preincubation for RPMs from ID mice. (Q) Flow cytometric assessment of EP capacity in RPMs of *Tmprss6* wt and *Tmprss6* KO mice quantified as the percentage of cells engulfing PKH67-labeled sRBCs. (R) Normalized EP capacity of PKH26 sRBCs by cultured iRPMs treated with serum from *Tmprss6* wt and *Tmprss6* KO mice determined using flow cytometry. Each dot represents one mouse or an independent cell-based experiment. Data are represented as mean ± SEM. Welch's unpaired t-test determined statistical significance in A-D and Q-R, while two-way ANOVA with Tukey's Multiple Comparison tests was used in G-O. A one-way ANOVA test with Dunnett's or Tukey's Multiple Comparison tests was used in E. In F, the significant differences between the slopes of simple linear regression lines are shown. ns $p>0.05$, *$p<0.05$, **$p<0.01$, ***$p<0.001$ and ****$p<0.0001$.

FPN overexpression induces EP and metabolic adaptation in an *in vitro* RPM cellular model

To further assess the role of FPN upregulation in RPM rewiring under systemic ID conditions, we used lentiviral transduction to create iRPMs with enforced FPN overexpression (FPN-iRPMs) and assessed whether this mimics RPM adaptation to iron deficiency. Control iRPMs were generated using an empty vector without the *Slc40a1* gene, encoding FPN (mock-iRPMs). We confirmed significant FPN elevation on the surface of FPN-iRPMs compared to control cells (Figure 4A). This further led to the elevation of TFR1 surface expression but did not significantly change the total iron levels (Figure 4B-C), thus resembling the iRPMs exposed to ID vs IB serum. Under basal conditions, we quantified the LIP in both FPN-iRPMs and mock-iRPMs, finding no significant

difference (Figure 4D). In an attempt to recapitulate the mildly elevated LIP observed in RPMs of ID mice during enhanced *in vivo* EP, we next sought to mimic the splenic microenvironment by continuously exposing iRPMs to sRBCs during culture. Strikingly, sRBC-exposed FPN-iRPMs exhibited a significant increase in LIP compared to mock-iRPMs, mirroring the *in vivo* RPM response (Figure 4D).. Most importantly, FPN-iRPMs displayed enhanced RBC clearance regardless of sRBC exposure during culture (Figure 4E). These findings demonstrate that forced FPN expression specifically stimulates EP, independently of iron status.

To investigate in more detail the potential metabolic consequences of increased FPN expression, we assessed mitochondrial activity and mass. FPN overexpression led to a significant increase in both mitochondrial activity and mass compared to mock-transfected iRPMs (Figure 4F-G). This effect was mirrored by a corresponding increase in glucose uptake and protein synthesis rate in FPN-overexpressing iRPMs (Figure 4H-I), suggesting a coordinated metabolic adaptation. Importantly, these responses were independent of the presence of sRBCs in the culture media and intracellular iRPM LIP levels (Figure S4A-D), indicating a regulatory effect of FPN on mitochondrial functions which may reach beyond its role as a regulator of intracellular iron status.

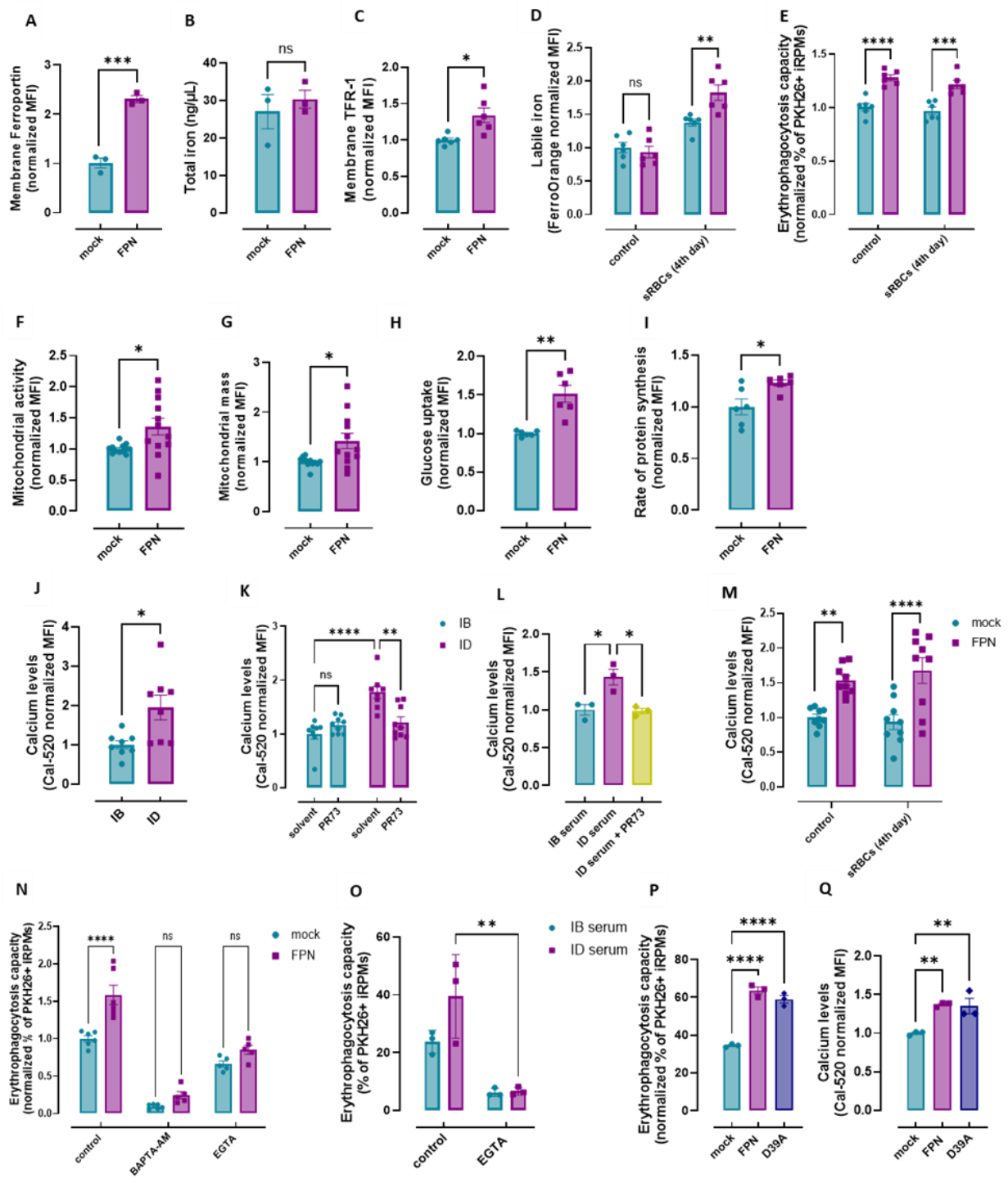

Figure 4: **Elevated ferroportin and increased intracellular Ca^{2+} levels regulate RPM phagocytic activities in ID conditions**

Lentiviral transduction was used to generate iRPMs overexpressing ferroportin (FPN-iRPMs) or expressing an empty vector (mock). (A) Flow cytometric analysis of ferroportin cell surface expression on mock and FPN-iRPMs. (B) Intracellular iron content in mock and FPN-iRPMs as determined using the Iron Assay Kit. (C) Flow cytometric evaluation of transferrin receptor 1 (TFR1) surface expression on mock and FPN-

371 iRPMs iRPMs. (D) Flow cytometric measurement of cytosolic ferrous iron (Fe2+) levels in mock and FPN-
372 iRPMs with and without sRBC exposure during culture. (E) Normalized EP capacity of PKH26-sRBCs by
373 mock and FPN-iRPMs with and without sRBC exposure. (F) Mitochondrial activity was determined in
374 mock and FPN-iRPMs with sRBC exposure using TMRE probe, with flow cytometry. (G) Mitochondrial
375 mass was determined in mock and FPN-iRPMs with sRBC exposure using MitoTracker Green, with flow
376 cytometry. (H) Quantification of glucose uptake via flow cytometry in mock and FPN-iRPMs with sRBCs
377 exposure using a fluorescent glucose analog. (I) Flow cytometric detection of newly synthesized proteins in
378 mock and FPN-iRPMs with sRBCs exposure using Click-iT Plus OPP Alexa Fluor 488 Protein Synthesis
379 Assay. (J) Cytosolic calcium iron (Ca^{2+}) levels in RPMs of IB and ID mice were measured using Cal-520
380 fluorescent probe with flow cytometry. (K) Cytosolic Ca^{2+} levels in RPMs of IB and ID mice were measured
381 with flow cytometry post-PR73 administration using Cal-520 fluorescent probe with flow cytometry. (L)
382 Cytosolic Ca^{2+} levels in iRPMs treated with serum from IB or ID mice and serum from ID mice treated with
383 the hepcidin agonist PR73 (50 nmol/mouse, 4 h) determined using Cal-520 fluorescent probe with flow
384 cytometry. (M) Flow cytometric measurement of cytosolic Ca^{2+} levels in mock and FPN-iRPMs with and
385 without sRBC exposure using Cal-520 fluorescent probe with flow cytometry. (N) Normalized EP capacity
386 of PKH26-sRBCs by mock and FPN-iRPMs treated with an intracellular (BAPTA-AM; 10 μM for 1 hour)
387 and extracellular (EGTA; 3mM for 30 minutes) calcium chelator. (O) The EP capacity in iRPMs treated
388 with serum from IB and ID mice, and serum from IB and ID mice treated with extracellular (EGTA; 3mM
389 for 30 minutes) calcium chelator determined using flow cytometry by measuring the percentage of cells that
390 phagocytosed transfused PKH26-labeled RBCs. (P) Flow cytometric assessment of EP capacity in mock,
391 FPN, and D39A-iRPMs quantified as the percentage of cells engulfing PKH26-labeled RBCs. (Q) Flow
392 cytometric measurement of cytosolic Ca^{2+} levels in mock, FPN, and D39A-iRPMs using Cal-520
393 fluorescent probe with flow cytometry. Each dot represents one mouse or an independent cell-based
394 experiment. Data are represented as mean ± SEM. Welch's unpaired t-test determined statistical significance
395 in A-C and F-J. Two-way ANOVA with Tukey's Multiple Comparison tests was used in D-E, K and M-O.
396 A one-way ANOVA test with Dunnett's or Tukey's Multiple Comparison tests was used in L and P-Q. ns
397 $p>0.05$, *$p<0.05$, **$p<0.01$, ***$p<0.001$ and ****$p<0.0001$.

398 **Increased intracellular Ca^{2+} levels regulate RPM phagocytic activities in ID conditions**

399 We next set out to elucidate the signaling mechanisms underlying the functional rewiring of RPMs
400 in response to increased FPN expression during systemic iron deficiency. Our previous work
401 demonstrated that age-related iron overload, likely due to low FPN expression suppressed RPM's
402 RBC clearance capacity. [21] This phenomenon was recapitulated in iron-loaded *in vitro* iRPMs and
403 was reflected by reduced intracellular Ca^{2+} levels, [21] a key regulatory signal for phagocytosis[52].
404 Inspired by this observation, we found a significant increase in intracellular Ca^{2+} levels within
405 RPMs of ID mice compared to IB mice (Figure 4J), mirroring the enhanced RBC clearance
406 capacity. PR73 administration reversed the elevated intracellular Ca^{2+} levels specifically in RPMs
407 of ID mice, with no effect observed in RPMs of IB mice (Figure 4K). In parallel, iRPMs exposed
408 to ID serum also displayed increased Ca^{2+} levels, a response likewise suppressed by PR73 treatment
409 (Figure 4L). This demonstrates that intracellular Ca^{2+} signaling, like phagocytic and mitochondrial
410 activities, is uniquely reprogrammed in RPMs of iron-restricted mice in a manner dependent on
411 low hepcidin. Consistently, FPN-iRPMs exhibited increased intracellular Ca^{2+} levels compared to

412 mock-iRPMs, independent of the presence of RBCs during culture and cellular LIP levels, further
413 implying the role of Ca^{2+} signaling in RPM functional rewiring driven by high FPN (Figure 4M).
414 To further examine whether enhanced Ca^{2+} signaling may support increased EP in RPM we
415 employed both intracellular (BAPTA-AM) and/or extracellular (EGTA) Ca^{2+} chelators in the FPN-
416 iRPM model and iRPMs exposed to ID and IB serum (Figure 4N-O). Both chelation strategies not
417 only reduced the overall EP capacity of iRPMs but also effectively suppressed the enhancement of
418 RBC clearance in FPN-high conditions, suggesting that FPN-mediated activation of Ca^{2+} signaling
419 contributes to enhanced phagocytic capacity of RPMs.

420 Recent findings implied that FPN may have the capacity for Ca^{2+} import[53]. To test whether FPN-
421 mediated Ca^{2+} influx directly drives their functional rewiring, we employed overexpression of the
422 FPN variant harboring a specific aspartate-to-alanine mutation (D39A), expected to disrupt the
423 unidirectional movement of Ca^{2+} into the cell while preserving Fe^{2+} transport function.
424 Interestingly, we found no significant differences in the enhancement of EP or intracellular Ca^{2+}
425 levels between iRPMs overexpressing mutant D39A and wild-type FPN (Figure 4P-Q), suggesting
426 an indirect impact of FPN on Ca^{2+} signaling.

427 **SYK kinase inhibition disrupts the adaptation of RPMs to ID conditions**

428 Expanding on prior knowledge, we next sought to identify the genetic mediators of Ca^{2+}-dependent
429 signaling underlying the functional rewiring of RPMs in ID mice. First, we examined the
430 involvement of the PIEZO1, a mechanoreceptor recently identified in a genetic mouse model to
431 modulate Ca^{2+} signaling and EP in RPMs[26]. Indeed, under basal conditions, treatment of iRPMs *in*
432 *vitro* with the PIEZO1 activator YODA1 and the inhibitor GsMTx1 mildly affected EP (Figure
433 S5A-B)). However, GsMTx1 did not significantly affect the enhanced EP capacity observed in
434 iRPMs exposed to ID serum (Figure S5C). These findings excluded a major role for PIEZO1 in
435 mediating the functional acceleration of RPMs in response to iron deficiency.

436 To further dissect the Ca^{2+}-dependent signaling pathways responsible for the enhanced EP observed
437 in RPMs during iron deficiency, we performed a targeted pharmacological screen. Inhibitors of
438 CaMKK (STO-609), calmodulin-mediated signaling (W7), P2 receptor-mediated Ca^{2+} signaling
439 (Apyrase)[54], and macropinocytosis (EIPA) had no discernible impact on EP in either mock or FPN-
440 iRPMs (Figure 5A). Likewise, despite its well-established role in Ca^{2+}-dependent signaling,
441 inhibition of protein kinase C (PKC) with Bisindolylmaleimide I did not reduce EP in either mock-

or FPN-iRPMs (Figure 5A). However, the inhibition of the spleen tyrosine kinase (SYK), a downstream effector of PKC-dependent signaling, with piceatannol completely abolished the increased EP in FPN-iRPMs vs mock-transduced iRPMs (Figure 5A). To mitigate the potential off-target effects of piceatannol, we next employed the highly selective SYK inhibitor entospletinib (ENTO; also known as GS-9973) in mock- and FPN-iRPM cultures. Consistently, ENTO effectively suppressed FPN-driven EP enhancement in FPN-iRPMs and iRPMs cultured in ID versus IB serum (Figure 5B-C). Furthermore, we observed that ENTO prevented an increase in Ca^{2+} levels upon FPN overexpression (Figure 5D). Interestingly, supplementation with ENTO was sufficient to reduce both the mitochondrial activity and mass of iRPMs overexpressing FPN to the control levels of mock-transduced cells (Figure 5E-F).

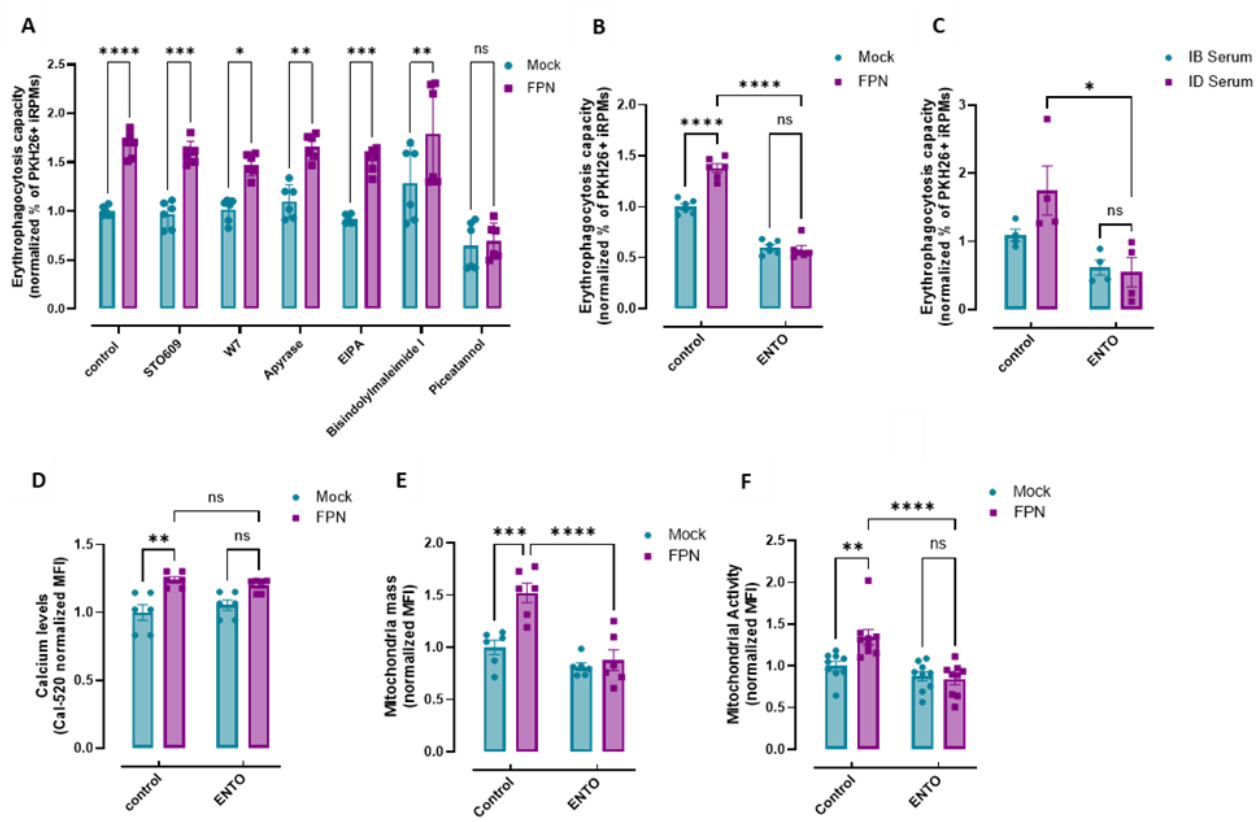

Figure 5. **SYK kinase mediates the FPN-dependent adaptation of RPMs to ID conditions**

All experiments were performed with exposure to sRBC. (A) Normalized EP capacity of mock and FPN-iRPMs, measured by uptake of PKH26-labeled sRBCs. iRPMs were analyzed with sRBC exposure and after treatment with inhibitors targeting CaMKK (STO-609), P2 receptor-mediated Ca^{2+} signaling (Apyrase), calmodulin (W7), macropinocytosis (EIPA), protein kinase C (Bisindolylmaleimide), and spleen tyrosine kinase (SYK; Piceatannol). (B) Normalized EP capacity of mock and FPN-iRPMs with and without treatment with SYK inhibitor Entospletinib (ENTO) measured by uptake of PKH26-labeled sRBCs. (C)

460 Normalized EP capacity of iRPMs cultured with serum from IB or ID mice with and without treatment with
461 ENTO measured by uptake of PKH26-labeled sRBCs. (D) Flow cytometric measurement of cytosolic Ca^{2+}
462 levels in mock and FPN-iRPMs with and without treatment with ENTO using Cal-520 fluorescent probe
463 with flow cytometry. (E) Mitochondrial mass was determined in mock and FPN-iRPMs with and without
464 treatment with ENTO using MitoTracker Green, with flow cytometry. (F) Mitochondrial activity was
465 measured in mock and FPN-iRPMs with and without treatment with ENTO using TMRE probe, with flow
466 cytometry. Each dot represents an independent cell-based experiment. Data are represented as mean ± SEM.
467 Two-way ANOVA with Tukey's Multiple Comparison tests was used to determine statistical significance.
468 ns $p>0.05$, *$p<0.05$, **$p<0.01$, ***$p<0.001$ and ****$p<0.0001$.

469 Next, we sought to investigate the role of SYK in RPM iron recycling *in vivo.* First, interestingly,
470 we found that a 4-hour treatment of ID mice with PR73 potently reduced phospho-SYK (Y525/526)
471 levels in RPMs, while no significant effect of the hepcidin agonist was observed in RPMs of IB
472 mice (Figure 6A), similarly to all previous ID-specific suppressive effects of PR73 on RPM
473 rewiring phenotypes. We further assessed the impact of the SYK inhibition with ENTO in both IB
474 and ID mice. Oral daily ENTO administration for the last 2 weeks of the iron-modified diet (5
475 mg/kg/day; with flavored jellies) effectively reduced phospho-SYK (Y525/526) levels in RPMs
476 from both IB and ID mice compared to vehicle controls (Figure 6B). Strikingly, ENTO
477 administration led to a marked reduction in the EP capacity of RPMs specifically in ID mice while
478 EP in IB mice remained unaffected by ENTO treatment (Figure 6C). Similarly, ENTO abrogated
479 an increase of Ca^{2+} levels in ID but not IB RPMs (Figure 6D). Interestingly, ENTO also suppressed
480 FPN induction associated with iron deficiency (Figure 6E), suggesting that EP capacity and FPN
481 expression may be bidirectionally linked. The modulation of FPN appeared as independent of liver
482 hepcidin mRNA expression, with no hepcidin induction observed by ENTO supplementation
483 (Figure 6F). On systemic levels, a 2-week ENTO treatment did not affect liver iron content (Figure
484 S6A) or hematological parameters in the circulating blood (Figure S6B-C), but it significantly
485 reduced transferrin saturation in both IB and ID mice (Figure 6G). Therefore, we extended the
486 period of ENTO administration for 3 weeks and evaluated the systemic blood parameters. We
487 observed that both Hb and MCH showed a significant, although modest, reduction in ENTO-
488 administered mice compared to vehicle control (Figure 6H-I)), indicating the onset of systemic
489 hematological effects with prolonged ENTO treatment. Consistently, whereas erythroid progenitors
490 expansion was not affected by ID in the bone marrow, we detected a more pronounced expansion
491 of immature splenic progenitors – in ENTO-treated vs control mice (Figure 6J). This suggests that
492 a more pronounced compensatory extramedullary erythropoietic response is initiated by ENTO
493 likely due to less effective iron delivery from iron-recycling RPMs.

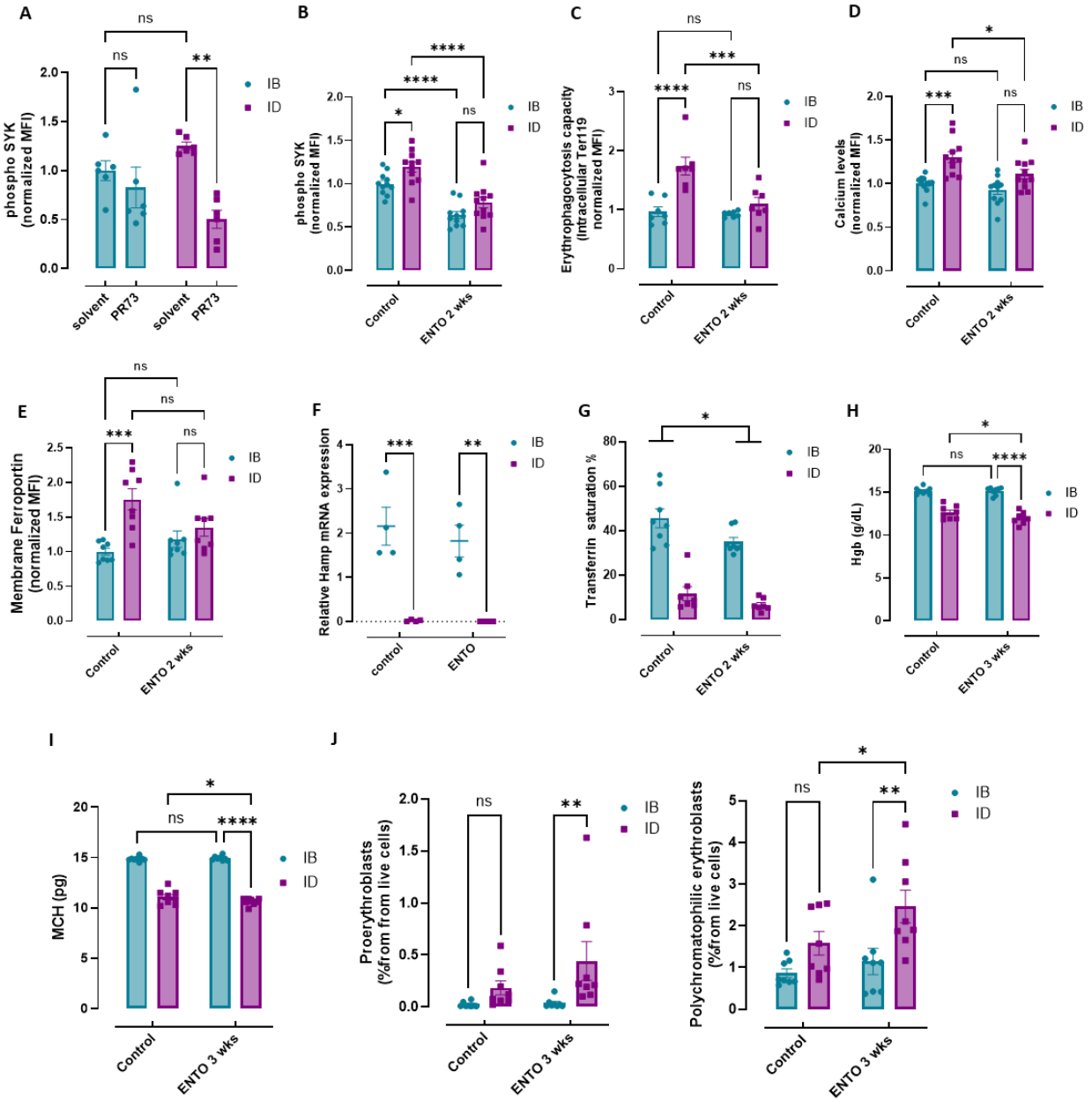

Figure 6. **SYK kinase inhibition disrupts the adaptation of RPMs to ID conditions in mice.**

(A) Flow cytometric analysis of phosphorylated SYK (phospho-SYK) in RPMs isolated from IB and ID mice, 4 hours after intraperitoneal administration of the hepcidin agonist PR73 (50 nmol/mouse). (B) Phospho-SYK levels in RPMs were assessed by flow cytometry in IB and ID mice after 2 weeks of intervention with or without ENTO jelly supplementation. (C) EP capacity of RPMs from IB and ID mice, determined by intracellular staining for the erythrocyte marker TER119 followed by flow cytometry, after 2 weeks of intervention with or without ENTO supplementation. (D) Cytosolic Ca^{2+} levels in RPMs from IB and ID mice, measured by flow cytometry using the Cal-520 fluorescent probe, with or without ENTO for 2 weeks. (E) Surface expression of ferroportin on RPMs assessed by flow cytometry in IB and ID mice following 2 weeks of supplementation with or without ENTO. (F) Relative mRNA expression of the Hamp gene in RPMs from IB and ID mice after 2 weeks of ENTO or control jelly supplementation. (G) Plasma

transferrin saturation levels were measured in IB and ID mice after 2 weeks of intervention with or without ENTO jelly. (H) Blood hemoglobin (Hb) concentration was determined in IB and ID mice following 3 weeks of dietary intervention with or without ENTO. (I) Mean corpuscular hemoglobin (MCH) values in IB and ID mice after 3 weeks of dietary intervention with or without ENTO supplementation. (J) Proerythroblasts and polychromatophilic erythroblasts representations in spleens of IB and ID mice after 3 weeks of dietary intervention with or without ENTO supplementation. Each dot represents one mouse. Data are represented as mean ± SEM. Two-way ANOVA with Tukey's Multiple Comparison tests was used to determine statistical significance. For (G), statistical significance was assessed based on the main effect of the column factor. ns $p>0.05$, *$p<0.05$, **$p<0.01$, ***$p<0.001$ and ****$p<0.0001$.

DISCUSSION

Iron deficiency is a complex physiological state with multifaceted implications. The precise quantitative thresholds defining its onset and the cell-type-specific molecular consequences including the identification of the most vulnerable cell types and the sequence of cellular dysfunction triggered by iron deficiency, remain poorly understood. Beyond its well-known systemic effects, including anemia or neuronal deficits[27,55,56], iron deficiency profoundly impacts immune cell function, with studies demonstrating impaired lymphocyte proliferation[57,58] and altered macrophage responses[28,29]. However, much of our understanding of macrophage iron metabolism comes from *in vitro* studies or models that may not fully capture the complexity of *in vivo* iron deficiency. The seemingly contradictory findings regarding the effects of iron depletion on macrophage inflammatory cytokine production *in vitro* versus *in vivo*[45,59,60] highlight the critical need for a more nuanced, cell-type-specific, and context-dependent understanding of iron's role in macrophage function. Specifically, how specialized iron-recycling cells like RPMs adapt to the metabolic stress of systemic iron deficiency remains a key open question.

RPMs from ID mice displayed classical markers of cellular iron depletion (increased TFR1, decreased ferritin), reflecting activation of the iron-responsive element/iron regulatory protein (IRE/IRP) system, a post-transcriptional regulatory mechanism that normally increases iron uptake and reduces iron storage and FPN-mediated export under iron-limiting conditions[17,61]. However, we observed increased FPN expression in RPMs of ID mice, despite proteomic analysis showing elevated IRP2 levels. This implies that suppressed hepcidin levels in iron deficiency, which relieve the dominant negative regulation of FPN, override any potential IRP2-mediated repression. Although RPM iron stores were low, elevated LIP and oxidative stress were increased, consistent with enhanced EP activity identified by our study. Intriguingly, this observation suggests that not sole LIP levels, but potentially other iron-related signals informing on the cellular iron status contribute to IRP2 stabilization in RPMs. The elevated FPN expression facilitates the export of

540 iron derived from engulfed RBCs, supporting the accelerated stress erythropoiesis in the spleen
541 during iron deficiency. These results reveal an adaptive mechanism in RPMs, prioritizing systemic
542 iron delivery over cellular iron retention during deficiency.

543 Emerging evidence links substantial metabolic reprogramming to efferocytosis. This is hallmarked
544 by altered amino acid utilization, particularly of arginine, methionine, and tryptophan, lactate
545 production, boosted PPP pathway, increased glucose uptake and glycolysis[8,9], fatty acid
546 oxidation[10], and, critically, enhanced mitochondrial respiration, acting in concert to sustain
547 energetically demanding efferocytosis and promote anti-inflammatory milieu[11,12]. While RPMs of
548 ID mice retain some of these metabolic traits, particularly enhanced oxidative phosphorylation,
549 multi-omics analyses reveal a distinct divergence from canonical efferocytic programs. For
550 example, key transporters and enzymes involved in arginine and tryptophan metabolism are absent
551 or uninduced. The established cellular response to iron deficiency, frequently modeled through
552 TFR1 disruption, involves a metabolic shift towards glycolysis, accompanied by mitochondrial
553 dysfunction, and impairments in the electron transport chain[62]. RPMs from ID mice display
554 enhanced mitochondrial function, increased mass and membrane potential, and upregulated
555 oxidative phosphorylation evidenced by proteomic and functional data. This unique, cell-type-
556 specific metabolic adaptation, absent in Kupffer cells and peritoneal macrophages, suggests that
557 RPMs are exceptional in adjusting their physiology to increased bioenergetic demand, imposed by
558 boosted iron recycling capability. Whether these responses are driven by the spleen's unique
559 microenvironment, potentially via signals from extramedullary erythropoiesis, remains to be
560 understood. Notably, real-time measurements using the Seahorse extracellular flux analyzer
561 demonstrated a marked elevation in oxygen consumption rate (OCR) in RPMs from iron-deficient
562 mice, directly confirming heightened mitochondrial respiratory capacity in these cells. The fact that
563 this exceptional response was acutely shut down by inhibition of FPN by PR73, together with
564 suppression of the glucose uptake or protein synthesis rate, points to a novel relationship between
565 FPN functionality and cellular metabolism, particularly in the context of enhanced efferocytic
566 activity. These novel findings were further confirmed by similar metabolic responses elicited solely
567 by FPN overexpression in the RPM *in vitro* model.

568 Our work further identified significantly elevated intracellular Ca^{2+} levels in RPMs of ID mice,
569 closely dependent on functional FPN and correlating with their enhanced EP capacity. While recent

570 studies have demonstrated that PKC activity can promote FPN exposure on the cell surface in type
571 2 diabetes and as a response to iron loading[63], our findings suggest that, in the context of iron
572 deficiency, increased FPN expression and elevated intracellular Ca^{2+} may represent parallel or
573 intersecting pathways that together facilitate enhanced EP. It is also plausible, that RPMs of ID
574 mice, characterized by low iron stores, but elevated LIP, additionally regulate FPN exposure on the
575 surface via Ca^{2+}-stimulated high PKC activity. Our data suggest no direct involvement of PKC in
576 mediating FPN-dependent and Ca^{2+}-triggered regulation of EP, at least using the cellular model of
577 RPMs. However, RPMs of ID mice treated by ENTO not only downmodulate EP but also FPN
578 surface levels and Ca^{2+}, which may represent a secondary response, possibly mediated by PKC
579 activity.

580 Our discovery that SYK drives EP in RPMs aligns with its emerging roles in diverse phagocytic
581 processes. Bian *et al*. demonstrated that SYK activation overrides Cd47-SIRPα-mediated "don't
582 eat me" signals to enable inflammation-driven clearance of "self" RBC[24]. Recent studies highlight
583 SYK as a critical mediator of microglial responses to amyloid-β (Aβ) plaques in Alzheimer's
584 disease, where SYK deficiency impairs Aβ phagocytosis[64,65]. Our work extends this observation
585 by identifying iron deficiency as a physiological trigger for SYK activation in RPMs, with
586 upstream regulation by the low hepcidin-high FPN. Furthermore, our work reveals SYK-dependent
587 metabolic-phagocytic coupling. Whereas previous findings rather link high SYK activity to
588 inhibition of mitochondrial respiration[66], we show that mitochondrial membrane potential and
589 mass, heightened by FPN overexpression, critically depend on SYK activity. Critically, our data
590 imply that SYK may represent a novel molecular switch for the regulation of efferocytic capacity,
591 a concept that requires further work.

592 Finally, the FPN-SYK-mediated rewiring of RPMs in iron deficiency does not resemble M1/M2-
593 like polarization. RPMs from ID mice exhibited an ambiguous pattern of surface marker alterations
594 indicating inflammatory swewing, and no clear regulation of anti or pro-inflammatory mediators
595 in omics data. They also employed a mixed functional phenotype: elevated ROS production, driven
596 by increased labile iron, characteristic of M1 macrophages, alongside enhanced oxidative
597 phosphorylation, mitochondrial biogenesis, and lysosomal activity, features typically associated
598 with M2 macrophages[67–73]. Together with the notion that enhanced EP in RPMs only partially
599 resembles previously reported adaptation mechanisms to efferocytosis, proposes that the

polarization state of RPMs in iron deficiency represents a new type of adaptation, whose resemblance in other macrophage types/environmental conditions opens an avenue for future investigations.

Methods

Mice

Female C57BL/6 J mice were utilized for the experiments and housed under specific pathogen-free (SPF) conditions at the Experimental Medicine Centre in Bialystok, Poland. These mice were provided with either a standard iron-balanced diet (200 mg/kg, SAFE U8958P; IB diet) or an iron-deficient diet (5.9 mg/kg, SAFE U8958P; ID diet) for 5 weeks, commencing at 4 weeks of age. 9-week-old *Tmprss6* wild-type and KO mice were provided by Dr. Delphine Meynard from INSERM, Toulouse, France. Upon arrival at the local facility at the International Institute of Molecular and Cell Biology (IIMCB), mice were acclimatized briefly before being sacrificed or subjected to further procedures, if required. Ms4a3Cre-RosaTdT reporter mice[38], obtained from Florent Ginhoux, were maintained at IIMCB. Female C57BL/6-Tg(UBC-GFP)30Scha/J (UBI-GFP/BL6) mice were kindly provided by Aneta Suwińska (Faculty of Biology, University of Warsaw, Poland). For primary cell cultures, C57BL/6 J mice were maintained in the SPF facility at the Mossakowski Medical Research Institute in Warsaw, Poland. All animal experiments and protocols were approved by the respective local ethical committees in Olsztyn and Warsaw, including the decisions: Uchwala 026, WAW2/015/2019, and WAW2/048/2020). Usage of Ms4a3Cre-RosaTdT reporter mice was approved by WAW2/126/2023. For PR73 administration, mice were intraperitoneally injected with 50 nmol of PR73 for 4 hours before being sacrificed. The procedure was approved by the local ethical committee in Warsaw (WAW2/150/2019). Experiments including SYK were covered by the permission: WAW2/068/2024.

Isolation of Single-Cell Suspensions from Murine Organs

Bone marrow cells were obtained by flushing the femurs and tibias with sterile HBSS (Gibco, 14025092) using a 25G needle. Following centrifugation at 600 x g for 10 minutes at 4°C, the pellet containing the isolated cells was collected for further processing. The spleen was harvested and homogenized by passage through a 70 µm cell strainer (pluriSelect, 43-50070-51). Before FACS sorting, the spleen was enzymatically digested with HBSS containing 1 mg/mL Collagenase D

629 (Roche, 11088882001) and 50 U/mL DNase I for 30 minutes at 37°C to facilitate cell dissociation.
630 The resulting cell suspension was then washed with cold HBSS and centrifuged at 600 x g for 10
631 minutes at 4°C. The harvested liver was perfused using Liver Perfusion Medium (Gibco,
632 17701038), followed by mincing and enzymatic digestion in Liver Digest Medium (Gibco,
633 17703034) at 37°C for 30 minutes. The digested liver tissue was then pressed through a 70 µm
634 strainer into HBSS. The resulting cell suspension was centrifuged at 50 g for 3 minutes to separate
635 the hepatocyte-enriched pellet, which was discarded. The supernatant, containing non-parenchymal
636 cells, was further centrifuged at 700 g for 15 minutes at 4°C. The resulting cell pellet was
637 resuspended in a solution of 5 mL PBS with 0.5% BSA and 5 mL of 50% Percoll (Cytiva, 17-0891-
638 01) diluted in PBS. This suspension underwent Percoll gradient centrifugation at 700 g for 30
639 minutes at 20°C to enrich specific cell populations. The peritoneal cavity was lavaged with HBSS
640 to collect peritoneal fluid. The retrieved fluid was then passed through a 70 µm strainer to remove
641 debris, followed by centrifugation at 600 x g for 10 minutes at 4°C to pellet the peritoneal cells.
642 Blood was collected via cardiac puncture into a heparin-coated tube. The cells were separated by
643 centrifugation at 400 g for 10 minutes at 4°C following a wash with HBSS. RBCs present in a
644 single-cell suspension were lysed using 1X RBC Lysis buffer (BioLegend, 420302) for 3 minutes
645 at room temperature. However, this step was excluded when analyzing erythroid cells and RBCs.
646 Following that, the cells were washed with 1X HBSS and centrifuged at 600g for 10 minutes at
647 4°C. The resulting pellet was processed for subsequent functional assays and antibody labeling.

648 **Generation of iRPMs**

649 Mononuclear cells were aseptically harvested from the femurs and tibias of mice and subsequently
650 cultured at a concentration of 0.5 X 10^6/1mL in RPMI-1640 medium (Gibco, 61870036)
651 supplemented with 10% FBS (Cytiva, SV30160.03), 1X Penicillin-Streptomycin (Gibco,
652 15140122), and 20 ng/mL of macrophage colony-stimulating factor (MCSF, BioLegend, 576406)
653 in a 5% CO_2 incubator at 37°C. On days 4 and 6 of culture, the medium was replaced with fresh
654 complete medium supplemented with 20 µM hemin (Sigma-Aldrich, 51280) and 10 ng/mL
655 interleukin-33 (IL-33) (BioLegend, 580506). All subsequent experiments were performed on day
656 8 of culture. For treatments, hemine (Sigma-Aldrich, 51280) solution was prepared with 0.15 M
657 NaCl containing 10% NH_4OH. For the phagocytosis assay, iRPMs were treated for 1 hour with 10
658 µM Entospletinib (Selleck, S7523), 24 hours with 100 µM deferoxamine (DFE, Sigma-Aldrich,

659 D9533), 30 minutes with 10 μM BAPTA/AM (CALBIOCHEM, 196419), 1 hour with 3 mM EGTA
660 (Sigma, E8145).

661 **Flow Cytometric Analysis and Cell Sorting**

662 Cell suspensions of spleens and livers at a concentration of approximately 1×10^7, along with
663 iRPMs were stained with LIVE/DEAD Fixable Aqua/Violet (Invitrogen, L34966/L34964)
664 following the manufacturer's instructions to identify dead cells. After extensive washing, Fc block
665 was added to the cells at a 1:100 dilution in FACS buffer and incubated at 4˚C for 10 minutes. The
666 cells were then stained with fluorophore-conjugated antibodies at a dilution of 1:100 to 1:400,
667 depending on the titration, in FACS buffer for 30 minutes at 4˚C. The cells were washed thoroughly
668 with FACS buffer and analyzed using flow cytometry. For the analysis of splenic RPM populations,
669 surface antibodies such as CD45 (Biolegend, 30-F11), CD45R/B220 (Biolegend, RA3-6B2), Ly-
670 6G/Ly-6C (Gr-1) (Biolegend, RB6-8C5), CD3 (Biolegend, 17A2), F4/80 (Biolegend, BM8),
671 CD11b (Biolegend, M1/70), and TREML4 (Biolegend, 16E5) were used. For erythroid cell
672 analysis, TER-119 (Biolegend) and CD71 (Biolegend, RI7217) were included. Meanwhile, the
673 analysis of liver KCs and iRPM populations involved the use of surface antibodies, including CD45
674 (Biolegend, 30-F11), F4/80 (Biolegend, BM8), and CD11b (Biolegend, M1/70). FPN detection
675 was performed using a non-commercial antibody that recognizes the extracellular loop of mouse
676 FPN (rat monoclonal, Amgen, clone 1C7) directly conjugated with Alexa488 (Alexa Fluor 488
677 Labeling Kit ab236553). To analyze RBCs, surface antibodies such as CD45 (Biolegend, 30-F11),
678 TER-119 (Biolegend), and CD71 (Biolegend, RI7217) were used. Lastly, the analysis of peritoneal
679 macrophages involved the use of surface antibodies, including CD45 (Biolegend, 30-F11), F4/80
680 (Biolegend, BM8), MHCII (Biolegend, M5/114.15.2), and CD11b (Biolegend, M1/70). Events
681 were acquired using Aria II (BD Biosciences) or CytoFLEX (Beckman Coulter) and were analyzed
682 using FlowJo or CytExpert, respectively. For RNA sequencing (RNA-seq) and ATP levels
683 quantification, RPMs were sorted into Trizol-LS (Invitrogen, 10296010) or assay buffer,
684 respectively, using an Aria II cell sorter (BD Biosciences) with an 85 μm nozzle.

685 **Functional Assays and Detection of Intracellular Fe^{2+} Iron**

686 To assess intracellular ROS levels, CellROX Deep Red Reagent (Invitrogen, C10422) was used,
687 and fluorescence was measured in the APC channel following the manufacturer's protocol. The
688 lysosomal activity was evaluated using the Lysosomal Intracellular Activity Assay Kit (Biovision,

689 K448) and fluorescence was measured in the FITC channel as directed by the manufacturer. To
690 measure mitochondrial activity, the tetramethylrhodamine ethyl ester (TMRE) fluorescent probe
691 (Sigma-Aldrich, 87917) was utilized at a concentration of 400 nM for 30 min at 37 °C, and the
692 fluorescence was measured in the PE channel. Mitochondrial mass was measured by fluorescence
693 levels upon staining with MitoTracker Green (Invitrogen, M7514) at 100 nM for 30 min at 37 °C
694 in the FITC channel. Calcium (Ca^{2+}) levels (FITC channel) were determined by using Cal-520 AM
695 probe (Abcam, ab171868) at 5 μM for 1 hour at room temperature. The intracellular ferrous iron
696 (Fe^{2+}) content was determined using FerroOrange (Dojindo, F374) through flow cytometric
697 analysis in the PE channel. The cells were surface-stained and incubated with 1 μM FerroOrange
698 dye in HBSS for 30 min at 37 °C. The analysis was performed directly via flow cytometry without
699 further washing, as previously described. Glucose uptake was measured using the Glucose Uptake
700 Capacity Assay Kit (Dojindo, UP03) and fluorescence was measured in the APC channel as per the
701 manufacturer's protocol. To perform intracellular staining, cells that had already been surface-
702 stained were fixed using 4% PFA and permeabilized with 0.5% Triton-X in PBS. The cells were
703 then stained with appropriate primary antibodies for 1 hr at 4°C, followed by a 30 min incubation
704 with Alexa Fluor 488 or Alexa Fluor 647 conjugated anti-Rabbit IgG (1:1000 Thermo Fisher, A-
705 21206). Afterward, the geometric mean fluorescence intensities (MFI) of the probes/target protein
706 levels were measured by flow cytometry using Aria II (BD Biosciences) or CytoFLEX (Beckman
707 Coulter). Data were then analyzed using FlowJo or CytExpert software, respectively. For the probes
708 that emitted in PE, TREML4 was excluded, and RPMs were gated as F4/80^{high} CD11b^{dim}. The MFI
709 of the adequate fluorescence minus one (FMO) control was subtracted from the samples' MFI to
710 quantify the data. The data were further normalized for analysis.

711 **ATP levels**

712 The levels of cellular ATP in FACS-sorted RPMs (10000 cells per sample) were measured using
713 the ATP Assay Kit (Sigma-Aldrich, MAK473) according to the manufacturer's instructions.

714 **Magnetic Sorting of RPMs**

715 60 x 10^6 cells were incubated for 15 minutes at 4°C in PBS containing 5% Normal Rat Serum
716 (Thermo Scientific, 10710C) and anti-CD16/32 antibody (Biolegend, 101320) in a 5 mL round
717 bottom tube. The cells were then labeled with anti-F4/80 (APC, Biolegend, 123116), anti-Ly-
718 6G/Ly-6C (Gr-1) (Biotin, Biolegend, 108403), anti-CD3 (Biotin, Biolegend, 100243), anti-mouse

719 Ly-6C (Biotin, Biolegend, 128003), and anti-B220 (Biotin, Biolegend, 103204) for 20 minutes at
720 4°C in the dark. The cells were washed with a cold PBS solution containing 2 mM EDTA and 0.5%
721 BSA (hereafter referred to as "sorting buffer") and centrifuged at 600 g for 10 minutes. The pellet
722 was resuspended in 400 μL of sorting buffer containing 50 μL of MojoSort Streptavidin Nanobeads
723 (Biolegend, 480016) and kept in the cold and dark for 15 minutes. After incubation, an additional
724 400 μL of sorting buffer was added to the cells, and the tube was placed on an EasyEights EasySep
725 Magnet (STEMCELL, 18103) for 7 minutes. The supernatant was transferred to a fresh 5 mL tube
726 and centrifuged at 600 g for 10 minutes. The pellet was resuspended in 100 μL of sorting buffer,
727 and 10 μL of MojoSort Mouse anti-APC Nanobeads (Biolegend, 480072) were added. The
728 suspension was gently pipetted and incubated for 15 minutes at 4°C in the dark. The tube was then
729 placed on a magnet for 7 minutes, and the supernatant was saved for analysis. The beads with
730 attached F4/80+ cells were washed with sorting buffer and counted under a light microscope with
731 a Neubauer chamber. The cells were pelleted and frozen in liquid nitrogen for further analysis.

732 **Measurement of Cellular Iron Levels**

733 To determine the levels of total iron in magnetically sorted RPMs, the Iron Assay Kit from Sigma-
734 Aldrich (MAK025) was employed by following the manufacturer's instructions. The volume of
735 buffers and reagents used in the measurement of total iron in RPMs were adjusted accordingly. The
736 absorbance at 593 nm was recorded using a Nanodrop ND-1000 Spectrophotometer from Thermo
737 Fisher Scientific. Iron concentrations in RPMs (ng/μL) were calculated from the standard curve
738 and then normalized to the number of cells in each sample.

739 ***In Vivo* RBC Lifespan**

740 A sterile solution of EZ-Link Sulfo-NHS Biotin (Thermo Fisher Scientific, 21217) was prepared
741 in PBS with a final concentration of 1 mg per 100 μL. The solution was then filtered through a 0.1
742 μm filter (Millipore, SLVV033RS). One day before the first blood collection, 100 μL of the sterile
743 Biotin solution was intravenously injected into the mice. Blood samples were collected from the
744 tail vein on days 0, 4, 11, 18, and 25, using heparinized capillaries to prevent clotting. RBCs were
745 separated by centrifugation at 400 g for 5 minutes at 4°C, and each sample was resuspended in 250
746 μL of HBSS containing 5% normal rat serum (Thermo Fisher Scientific). The suspension was then
747 mixed with 2 μL of fluorescently labeled anti-TER-119 and streptavidin, except for the
748 fluorescence minus one (FMO) sample in each group where fluorescent streptavidin was omitted.

749 After incubation at 4°C for 30 minutes, the samples were centrifuged and resuspended in HBSS.
750 Flow cytometry was used to determine the percentage of biotinylated erythrocytes.

751 **Preparation of Stressed RBCs for Erythrophagocytosis Assays**

752 The preparation and staining of stressed RBCs followed a previously outlined procedure. To obtain
753 the RBCs, mice were humanely euthanized, and whole blood was aseptically collected via cardiac
754 puncture into CPDA-1 solution (Sigma-Aldrich, C4431) with a final concentration of 10%. The
755 collected whole blood was combined, and plasma was separated by centrifugation at 400 g for 15
756 min at 4°C, then filtered through a 0.1 μm filter and stored at 4°C. The RBCs were then suspended
757 in HBSS, and leukocytes were eliminated using Lymphosep (Biowest, L0560-500). Following this,
758 the cells were subjected to a 30-minute heating period at 48°C with continuous agitation to generate
759 stressed RBCs. To stain the sRBCs, 1×10^{10} RBCs were resuspended in 1 ml of diluent C and mixed
760 with 1 ml of diluent C containing 4 μM of PKH-67 (Sigma-Aldrich, MINI67) or PKH-26 (Sigma-
761 Aldrich, MINI26). The mixture was then incubated in the dark for 5 min at 37°C, and the reaction
762 was stopped by adding 10 mL of HBSS containing 2% FCS and 0.5% BSA. Staining was followed
763 by two washing steps with HBSS. For *in vitro* EP assays, the cells were resuspended in RPMI-1640
764 and counted. For the *in vivo* approach, RBCs were resuspended to 50% hematocrit in previously
765 collected and filtered plasma.

766 ***In Vitro* Erythrophagocytosis**

767 On the 8th day post-seeding, stained, and counted sRBCs were added to iRPMs on 12-well plates
768 in 10-fold excess for 1.5 hours at 37 °C and 5% CO_2. After incubation, the cells were extensively
769 washed with cold HBSS to eliminate any non-engulfed sRBCs. Subsequently, the cells were
770 detached using Accutase (BioLegend, 423201), which were then transferred to a round-bottom
771 FACS tube, washed with HBSS, and centrifuged at 600 g for 5 minutes. The cells were labeled
772 with antibodies and analyzed using flow cytometry. For time-lapse confocal imaging of the
773 execution of RBC uptake by iRPMS, sRBCs were stained with pH-sensitive pHrodo™ Deep Red
774 Mammalian and Bacterial Cell Labeling Kit. The imaging was performed using The Opera Phenix
775 (PerkinElmer), an automated confocal spinning disk microscope. Imaging was conducted for 120
776 min, with acquisition every 1.3 min.

777 ***In Vivo* Erythrophagocytosis**

778 The mice were intravenously transfused with 100 μL of RBCs resuspended in plasma to 50%
779 hematocrit. The animals were kept in cages with ad libitum access to food and water for 1.5 hours
780 before being sacrificed for organ isolation.

781 **Mini-Hepcidin (PR73) Preparation**

782 An optimized protocol was developed for preparing mini-Hepcidin (PR73, a kind gift from
783 Elizabeta Nemeth, UCLA, USA) for intraperitoneal injection in mice. Commercially available
784 PR73 powder may not represent the pure peptide, so we adjusted the preparation based on the
785 estimated active component content (80%). The process began by precisely weighing the PR73
786 powder to account for the estimated 80% active component. This powder was then dissolved in
787 80% ethanol to ensure complete extraction of the peptide. The solution was thoroughly mixed using
788 a vortex mixer to achieve a homogenous suspension. Next, the solution was carefully transferred
789 to a sterile, low-bind vial (SL-220) to minimize potential losses due to adsorption during
790 incubation. A brief heat treatment at 37°C for a few seconds facilitated the complete dissolution of
791 any undissolved particles. Following the heat treatment, the vial cap was removed, and the solution
792 was aliquoted into designated culture tubes for individual injections. A Speedvac concentrator was
793 then used to evaporate the ethanol, resulting in a concentrated PR73 gel within each tube. To
794 achieve a final working concentration of 1 nmol/μl, 1 ml of sterile, injectable-grade water was
795 added to each tube containing the PR73 gel. The tubes were vigorously vortexed to ensure complete
796 dissolution of the gel and homogenization of the solution. For *in vivo* experiments, 100 μl of the
797 prepared PR73 stock solution was administered per mouse via intraperitoneal injection. A solvent
798 control solution was prepared by following the same steps outlined above but substituting the PR73
799 solution with only 80% ethanol. This control solution served as a baseline for comparison with the
800 PR73-treated mice in subsequent experiments.

801 **Metabolic Flux Seahorse Assay**

802 Metabolic flux was assessed using a Seahorse XF-96 Extracellular Flux Analyzer (Agilent
803 Technologies) Mito Stress Test (Agilent,103010-100). Magnetically sorted RPMs (1×10^5
804 cells/well) from IB and ID mice were plated onto poly-L-lysine coated Seahorse XF HS Miniplates
805 (Agilent, 103725-100). Cells were incubated in Seahorse XF RPMI medium (Agilent, 103576-100)
806 supplemented with 2 mM L-glutamine (Agilent, 103579-100), 1 mM sodium pyruvate (Agilent,
807 103578-100), and 25 mM glucose (pH adjusted to 7.4; Agilent 103577-100) at 37°C in a non-CO_2

808 incubator for 60 minutes. Real-time oxygen consumption rate (OCR) was measured under basal
809 conditions and following sequential injections of 1 μM oligomycin, 1 μM FCCP, and a mixture of
810 1 μM rotenone and 1 μM antimycin A.

811 **Voluntary Oral Drug Administration**

812 Strawberry-flavored gelatin jellies were prepared under sterile conditions in 96-well plates (100
813 μL/well), with or without ENTO. Gelatin (8% w/v, Sigma-Aldrich, G9391) was dissolved in warm,
814 sterile water, and strawberry flavoring essence (1% v/v, OstroVit, 5903933916217) was added. Just
815 prior to gelation, ENTO was added to the appropriate wells of a sterile 96-well plate to achieve the
816 desired final concentration, while control wells received vehicle only. The gelatin solution (100
817 μL) was then added to each well, and plates were refrigerated at 4°C until solid. To acclimate IB
818 and ID mice, two drug-free jellies were provided per cage daily for 2-3 days (two mice per cage).
819 This co-housing approach minimized stress associated with individual training. Following
820 acclimation, mice readily consumed the jellies within 15-20 minutes. Drug-containing jellies were
821 administered at approximately the same time each day for two weeks.

822 **Generation of Ferroportin Overexpressing iRPMs**

823 We successfully cloned the wild-type *Slc40a1* gene, encoding mouse ferroportin (FPN; Uniport
824 ID: Q9JHI9), into the HIV SFFV lentiviral vector. Lentiviral production involved transfecting the
825 chosen lentiviral vectors (FPN, or Mock) along with the psPAX2 packaging vector and the
826 pMD2.G envelope vector into HEK293T cells. The resulting viral supernatants were harvested and
827 titrated to determine viral concentration. Subsequently, iRPMs were transduced with the lentiviral
828 vectors at a multiplicity of infection (MOI) of 1. This MOI ensured efficient transduction while
829 minimizing potential cytotoxicity. Expression levels of surface FPN were measured in each
830 experiment using flow cytometry. This verification step confirmed successful FPN overexpression
831 in my iRPM population, allowing for functional analysis of the consequences in subsequent
832 experiments.

833 **Hepcidin Measurement with ELISA**

834 Serum hepcidin levels were measured using the Hepcidin-Murine Compete ELISA Kit (Intrinsic
835 LifeSciences, HMC-001) following the manufacturer's instructions. Optical density was
836 determined with a microplate reader at a wavelength of 450 nm.

837 **Erythropoietin (EPO) Measurement with ELISA**

838 Serum EPO levels were measured using the Mouse Erythropoietin/EPO Quantikine ELISA Kit
839 (R&D Systems, MEP00B) following the manufacturer's instructions. Optical density was
840 determined with a microplate reader at a wavelength of 450 nm.

841 **Transferrin Saturation and Tissue Iron Measurements**

842 The levels of serum iron and unsaturated iron-binding capacity were quantified using SFBC
843 (Biolabo, 80008) and UIBC (Biolabo, 97408) kits per the manufacturer's instructions. Transferrin
844 saturation was determined using the formula SFBC/(SFBC+UIBC) x 100. Tissue non-heme iron
845 content was measured using the bathophenanthroline method and the results were calculated based
846 on tissue dry weight, as previously described[74].

847 **RT-qPCR**

848 RNA from cell pellets was isolated using an RNA purification kit (Eurex) according to the
849 manufacturer's instructions. RNA from liver tissue was isolated using TRIzol™ reagent according
850 to the manufacturer's instructions. 400 ng of RNA was subjected to reverse transcription. In the
851 first stage of the reaction, RNA was denatured, and random primers were attached. For this purpose,
852 a mixture consisting of 400 ng RNA, 1 µl of random primers at a concentration of 200 ng/µl, and
853 nuclease-free water was prepared so that the total reaction volume was 17.7 µl. The mixture was
854 incubated at 70°C for 10 minutes and then cooled to 4°C. The next step was to add the reaction
855 mixture to the tubes, which contained: 0.3 µl RevertAid H Minus reverse transcriptase, 1 µl of 10
856 mM dNTP solution, and 5 µl of reaction buffer. The total reaction volume was 25 µl. The reaction
857 was carried out for 60 minutes at 42°C, 70°C, 10 minutes. The obtained cDNA was diluted 9x and
858 then used for quantitative polymerase chain reaction (qPCR). The reaction mixture consisted of 4
859 µl cDNA, 7.5 µl SG qPCR Master Mix (2x), and 1.5 µl of a 5 µM solution of forward and reverse
860 primers. The whole was supplemented with nuclease-free water to a final reaction volume of 15 µl.
861 The qPCR reaction was carried out using the LightCycler 96 Real-Time PCR System (Roche). The
862 reaction was pre-incubated at 95°C for 600 s and then two-step amplification was performed 40x
863 (95°C x 15 s, 60°C x 60 s).

864 **Immunohistochemistry of Spleen Tissues**

865 The spleen was fixed in 4% PFA at 4°C for 24 h. Tissues were washed with PBS (3x30min) and
866 incubated for 2 h in 12.5% and then in 25% sucrose solution for 48 h. Subsequently, spleen tissue
867 fragments were embedded in the Cryomatrix medium, frozen in liquid nitrogen, and cut into 10 µm
868 thick sections using a cryo microtome (Leica). The sections were mounted on glass slides and
869 stored at -20°C. Before staining, the sections were warmed at room temperature for 30 min, and
870 then their edges were surrounded using a Pap Pen Liquid Blocker. Next, the slides with sections
871 were washed in PBS for 10 min and permeabilized in 0.1% Triton X-100 solution for 20 min.
872 Nonspecific antibody binding was blocked by incubating the sections in 3% BSA solution for 1 h
873 at room temperature. To visualize RPMs, the tissues were incubated with FITC-conjugated F4/80
874 antibody (1:100), and for FPN, with Alexa Flor 647-conjugated FPN antibody (1:100) in 3% BSA
875 for 2 h at room temperature in the dark. After incubation with antibodies, the tissues were washed
876 5 x 5 min in 0.1% Triton X-100 solution to remove unbound antibodies. To stain cell nuclei, the
877 sections were incubated with Hoechst 33342 diluted in 0.1% Triton X-100 solution (final
878 concentration - 1 µg/ml) for 10 min at room temperature in the dark. Then, the sections were
879 washed for 3 x 5 min in 0.1% Triton X-100 solution, incubated in PBS for 10 min, and mounted
880 with a coverslip using ProLong™ Glass Antifade Mountant. Samples were imaged on a confocal
881 microscope with a Plan-Apochromat 40x/1.3 NA oil immersion objective (Zeiss) LSM 800.

882 **Histological and Histochemical Analysis**

883 Following fixation in 10% formalin for 24 h, spleens were stored in 70% ethanol before further
884 preparation. The tissue was embedded in paraffin and 7 µm cross-sections were cut with a
885 microtome (Reichert-Jung, Germany). Sections were prepared as described above. After mounting
886 on glass slides, sections were deparaffinized, incubated with a working solution containing Perls'
887 Prussian Blue for 30 min, counterstained with pararosaniline solution for 2 min, and analyzed under
888 standard light microscopy (Olympus CH2).

889 **Proteomic analysis of RPMs**

890 <u>Sample Preparation</u>

891 Magnetically isolated RPMs were obtained from the spleens of IB and ID female C57BL/6J mice.
892 The cells were lysed using RIPA buffer. Proteins were precipitated using a chloroform/methanol

893 method, washed with methanol, and reconstituted in 100 mM HEPES (pH 8.0) containing 10 mM
894 TCEP and 10 mM chloroacetamide.

895 LC-MS/MS Analysis

896 10 µg of each lysate was subjected to an in-solution tryptic digest using a modified version of the
897 Single-Pot Solid-Phase-enhanced Sample Preparation (SP3) protocol[75,76]. To this end, lysates were
898 added to Sera-Mag Beads (Thermo Scientific, #4515-2105-050250, 6515-2105-050250) in 10 µl
899 15% formic acid and 30 µl of ethanol. The binding of proteins was achieved by shaking for 15 min
900 at room temperature. SDS was removed by 4 subsequent washes with 200 µl of 70% ethanol.
901 Proteins were digested overnight at room temperature with 0.4 µg of sequencing grade modified
902 trypsin (Promega, V5111) in 40 µl Hepes/NaOH, pH 8.4 in the presence of 1.25 mM TCEP and 5
903 mM chloroacetamide (Sigma-Aldrich, C0267). Beads were separated and washed with 10 µl of an
904 aqueous solution of 2% DMSO, and the combined eluates were dried down.

905 Up to 10 µg of peptides per sample were labeled with TMT10plex™ reagents following established
906 protocols[77]. Briefly, 0.8 mg of TMT reagent was dissolved in 45 µL of anhydrous acetonitrile, and
907 4 µL of this solution was added to each peptide sample. Labeling was carried out at room
908 temperature for 1 hour. The reaction was quenched by adding 4 µL of 5% hydroxylamine in water,
909 followed by a 15-minute incubation at room temperature. Labeled peptides were pooled for
910 multiplexing, desalted using an Oasis® HLB µElution Plate (Waters #186001828BA) according to
911 the manufacturer's instructions, and dried by vacuum centrifugation.

912 Offline high-pH reversed-phase fractionation was performed as described previously[78], using an
913 Agilent 1200 Infinity HPLC system equipped with a Gemini C18 analytical column (3 µm particle
914 size, 110 Å pore size, 100 × 1.0 mm; Phenomenex) and a matching Gemini C18 SecurityGuard pre-
915 column (4 × 2.0 mm; Phenomenex). Peptides were separated at a flow rate of 0.1 mL/min using
916 mobile phase A (20 mM ammonium formate, pH 10.0) and mobile phase B (100% acetonitrile).
917 The chromatographic gradient was as follows: 100% A for 2 min, linear increase to 35% B over
918 59 min, ramp to 85% B in 1 min, held at 85% B for 15 min, followed by re-equilibration at 100%
919 A for 13 min. A total of 48 fractions were collected and subsequently pooled into 12 final fractions.
920 Nanoflow LC-MS/MS analysis was performed on an UltiMate 3000 RSLCnano system (Thermo
921 Fisher Scientific) coupled to an Orbitrap Fusion™ Lumos™ Tribrid™ mass spectrometer (Thermo
922 Fisher Scientific). Peptides were initially loaded onto a µ-Precolumn C18 PepMap™ 100 trap

923 cartridge (300 µm i.d. × 5 mm, 5 µm particles, 100 Å; Thermo) at 30 µL/min with 0.05% TFA in
924 water for 6 min. Analytical separation was carried out using a nanoEase™ M/Z HSS T3 column
925 (75 µm i.d. × 250 mm, 1.8 µm particles, 100 Å; Waters), equilibrated with solvent A (3% DMSO,
926 0.1% formic acid in water). Peptides were eluted at 0.3 µL/min using a gradient of solvent B (3%
927 DMSO, 0.1% formic acid in acetonitrile) as follows: 2–8% B over 6 min, 8–25% over 99 min, 25–
928 40% over 5 min, ramp to 85% in 0.1 min, held at 85% for 3.9 min, followed by re-equilibration to
929 2% B for 6 min. Mass spectrometry was performed using a Pico-Tip emitter (360 µm OD × 20 µm
930 ID, 10 µm tip; CoAnn Technologies) with a spray voltage of 2.4 kV and a capillary temperature of
931 275 °C. Full MS scans were acquired in the Orbitrap at a resolution of 120,000 (at m/z 200), over
932 a mass range of m/z 375–1,500, with an AGC target set to 'standard' and a maximum injection time
933 of 50 ms. The instrument operated in data-dependent acquisition (DDA) mode. MS/MS spectra
934 were acquired in the Orbitrap at a resolution of 30,000, with a maximum injection time of 94 ms
935 and an AGC target of 200%. Precursors were fragmented using higher-energy collisional
936 dissociation (HCD) at 36% normalized collision energy. A quadrupole isolation window of 0.7 m/z
937 was used, with dynamic exclusion set to 60 s. Only precursor ions with charge states between 2
938 and 7 were selected for fragmentation.

939 Acquired data were analyzed using IsobarQuant and Mascot V2.4 (Matrix Science) using a reverse
940 UniProt FASTA Mus musculus database (UP000000589) including common contaminants. The
941 following modifications were considered: Carbamidomethyl (C, fixed), TMT10plex (K, fixed),
942 Acetyl (N-term, variable), Oxidation (M, variable), and TMT10plex (N-term, variable). The mass
943 error tolerance for full scan MS spectra was set to 10 ppm and for MS/MS spectra to 0.02 Da. A
944 maximum of 2 missed cleavages were allowed. A minimum of 2 unique peptides with a peptide
945 length of at least seven amino acids and a false discovery rate below 0.01 were required on the
946 peptide and protein level.

947 Data Processing

948 The data were processed using MaxQuant 2.1.3.0, with peptides identified from MS/MS spectra
949 searched against the Uniprot Mouse Reference Proteome (UP000000589) using the built-in
950 Andromeda search engine. Fixed modifications included cysteine carbamidomethylation, while
951 variable modifications included methionine oxidation, glutamine/asparagine deamination, and
952 protein N-terminal acetylation. In silico digests allowed for cleavages of arginine or lysine followed

953 by any amino acid (trypsin/P), with up to two missed cleavages permitted. The false discovery rate
954 (FDR) was set to 0.01 for peptides, proteins, and sites. Match between runs was enabled, and other
955 parameters were used as preset in the software. Protein identification and intrasample
956 quantification were performed using the iBAQ algorithm in MaxQuant.

957 **Transmission Electron Microscopy (TEM) of the Spleen**

958 Fresh spleen samples, approximately 3 mm^2 in size, were fixed in 2.5% glutaraldehyde for 24 hours
959 at 4°C. Following fixation, the samples were washed in PBS and postfixed with 1% osmium
960 tetroxide for 1 hour. After rinsing with water, the samples were incubated in 1% aqueous uranyl
961 acetate for 12 hours at 4°C. The samples were then dehydrated at room temperature using
962 increasing concentrations of ethanol, infiltrated with epoxy resin (Sigma-Aldrich, 45-359-1EA-F),
963 and polymerized for 48 hours at 60°C. The polymerized resin blocks were trimmed using a tissue
964 processor (Leica EM TP) and sectioned into ultrathin slices (65 nm thick) with an ultramicrotome
965 (EM UC7, Leica). These ultrathin sections were collected on nickel grids with 200 mesh (Agar
966 Scientific, G2200N). The specimen grids were examined with a Tecnai T12 BioTwin transmission
967 electron microscope (FEI, Hillsboro, OR, USA) equipped with a 16-megapixel TemCam-F416
968 camera (TVIPS GmbH) at the in-house Microscopy and Cytometry Facility.

969 **Preparation of Schematic Figures**

970 Schematic figures were prepared based on cited literature or own results using the online program
971 BioRender, available at https://www.biorender.com.

972 **Statistical Analysis**

973 Female mice of the same age were randomly assigned to experimental groups, either based on iron
974 diet, PR73 and ENTO administration, or *Tmprss6* KO. Samples derived from these mice were
975 collected randomly within groups, assessed/measured randomly, and harvested in a different order
976 across individual experiments. The sample size, typically ranging from 5 to 9 mice per group or
977 independent biological cell-based experiments, was determined based on power analysis, prior
978 experience with similar experiments, and previously published studies in the field of RPM biology.
979 Statistical analysis was conducted using GraphPad Prism (GraphPad Software, Version 9). Data
980 are presented as mean ± SEM unless otherwise noted. Student's t-test with Welch's correction was
981 employed when comparing the two groups. For comparisons involving more than two groups, one-

982 way ANOVA was used, or two-way ANOVA when the simultaneous effects of two factors were
983 being evaluated. Tukey's test was implemented for post-hoc analysis following ANOVA. The
984 following notation was used to indicate statistically significant differences between means: ns for
985 non-significant ($p > 0.05$), * for $p < 0.05$, ** for $p < 0.01$, *** for $p < 0.001$, and **** for $p <$
986 0.0001.

987 **Data availability**

988 Mass spectrometry proteomics data were deposited to the ProteomeXchange Consortium via the
989 PRIDE partner repository with the dataset identifiers: Project accession: PXD064719 (access
990 secured by a token: lKilHQArXhhB. RNA sequencing data are deposited to the NCBI BioSample
991 repository (under accession no: SAMN48982825, SAMN48982826, SAMN48982827,
992 SAMN48982828, SAMN48982829, SAMN48982830, SAMN48982831, SAMN48982832).

993 **Authorship Contributions**

994 KMS, PKM, PS, RM, and KC conceived and planned the experiments; PKM, PS, RM, KC, GZ,
995 MN, AJ, and ML performed research; PKM, PS, RM, KC, GZ, KMS and ML analyzed and
996 visualized data; EN and DM provided critical reagents/models, KC and KMS curated data; KMS,
997 WP, and EN supervised the study; KC and RM edited the manuscript, PKM and KMS wrote the
998 manuscript.

999 **Conflict of interest**

1000 EN is a shareholder and scientific advisor of Intrinsic LifeSciences and Silarus Therapeutics, and
1001 a consultant for Disc Medicine, Ionis Pharmaceuticals, Protagonist, GSK and Vifor. Other authors
1002 have declared that no conflict of interest exists.

1003 **Acknowledgments**

1004 We thank the EMBL Proteomics Core Facility (EMBL, Heidelberg) for performing RPM proteomic
1005 profiling and data analysis. We thank Tara Arvedson (Amgen Inc.Inc, USA) for the anti-ferroportin
1006 antibody, Elizabeta Nemeth (UCLA, USA) for PR73, Florent Ginhoux for access to Ms4a3-Cre
1007 mice, and Aneta Suwińska for sharing UBI-GFP/BL6 mice. Many thanks to Agnieszka Popielska
1008 and Anna Kosson, and the staff of the Experimental Medicine Centre (Bialystok, Poland) and
1009 Mossakowski Medical Research Institute (Warsaw, Poland) for their technical support. We thank

Sylwia Herman for her assistance in histological analyses. This research was performed thanks to the IIMCB IN-MOL-CELL Infrastructure (RRID: SCR_021630) funded by the European Union–NextGenerationEU under the National Recovery and Resilience Plan. IN-MOL-CELL Infrastructure was also funded by the European Union under Horizon Europe (Project 101059801 - RACE) and by the RACE-PRIME project carried out within the IRAP program of the Foundation for Polish Science co-financed by the European Union under the European Funds for Smart Economy 2021-2027 (FENG). Pratik Kumar Mandal gratefully acknowledges funding from the National Science Centre PRELUDIUM 22 grant which supported experiments involving lentiviral-mediated FPN overexpression (UMO-2023/49/N/NZ3/04232). This work was funded by the National Science Centre Sonata Bis grant (UMO-2020/38/E/NZ4/00511).

REFERENCES

1. Boada-Romero, E., Martinez, J., Heckmann, B.L., and Green, D.R. (2020). The clearance of dead cells by efferocytosis. Nat Rev Mol Cell Biol *21*, 398–414. https://doi.org/10.1038/s41580-020-0232-1.

2. Doran, A.C., Yurdagul, A., and Tabas, I. (2020). Efferocytosis in health and disease. Nat Rev Immunol *20*, 254–267. https://doi.org/10.1038/s41577-019-0240-6.

3. Moon, B., Yang, S., Moon, H., Lee, J., and Park, D. (2023). After cell death: the molecular machinery of efferocytosis. Exp Mol Med *55*, 1644–1651. https://doi.org/10.1038/s12276-023-01070-5.

4. Sheng, Y.R., Hu, W.T., Chen, S., and Zhu, X.Y. (2024). Efferocytosis by macrophages in physiological and pathological conditions: regulatory pathways and molecular mechanisms. Front Immunol *15*, 1275203. https://doi.org/10.3389/fimmu.2024.1275203.

5. Mukundan, L., Odegaard, J.I., Morel, C.R., Heredia, J.E., Mwangi, J.W., Ricardo-Gonzalez, R.R., Goh, Y.P.S., Eagle, A.R., Dunn, S.E., Awakuni, J.U.H., et al. (2009). PPAR-delta senses and orchestrates clearance of apoptotic cells to promote tolerance. Nat Med *15*, 1266–1272. https://doi.org/10.1038/nm.2048.

6. A-Gonzalez, N., Bensinger, S.J., Hong, C., Beceiro, S., Bradley, M.N., Zelcer, N., Deniz, J., Ramirez, C., Díaz, M., Gallardo, G., et al. (2009). Apoptotic cells promote their own clearance and immune tolerance through activation of the nuclear receptor LXR. Immunity *31*, 245–258. https://doi.org/10.1016/j.immuni.2009.06.018.

7. Mota, A.C., Dominguez, M., Weigert, A., Snodgrass, R.G., Namgaladze, D., and Brüne, B. (2021). Lysosome-Dependent LXR and PPARδ Activation Upon Efferocytosis in Human Macrophages. Front Immunol *12*, 637778. https://doi.org/10.3389/fimmu.2021.637778.

1043 8. Schilperoort, M., Ngai, D., Katerelos, M., Power, D.A., and Tabas, I. (2023). PFKFB2-
1044 mediated glycolysis promotes lactate-driven continual efferocytosis by macrophages. Nat
1045 Metab *5*, 431–444. https://doi.org/10.1038/s42255-023-00736-8.

1046 9. Morioka, S., Perry, J.S.A., Raymond, M.H., Medina, C.B., Zhu, Y., Zhao, L., Serbulea, V.,
1047 Onengut-Gumuscu, S., Leitinger, N., Kucenas, S., et al. (2018). Efferocytosis induces a novel
1048 SLC program to promote glucose uptake and lactate release. Nature *563*, 714–718.
1049 https://doi.org/10.1038/s41586-018-0735-5.

1050 10. Zhang, S., Weinberg, S., DeBerge, M., Gainullina, A., Schipma, M., Kinchen, J.M., Ben-
1051 Sahra, I., Gius, D.R., Yvan-Charvet, L., Chandel, N.S., et al. (2019). Efferocytosis Fuels
1052 Requirements of Fatty Acid Oxidation and the Electron Transport Chain to Polarize
1053 Macrophages for Tissue Repair. Cell Metab *29*, 443-456.e5.
1054 https://doi.org/10.1016/j.cmet.2018.12.004.

1055 11. Wang, Y., Subramanian, M., Yurdagul, A., Barbosa-Lorenzi, V.C., Cai, B., de Juan-Sanz, J.,
1056 Ryan, T.A., Nomura, M., Maxfield, F.R., and Tabas, I. (2017). Mitochondrial Fission
1057 Promotes the Continued Clearance of Apoptotic Cells by Macrophages. Cell *171*, 331-
1058 345.e22. https://doi.org/10.1016/j.cell.2017.08.041.

1059 12. Jiang, S., Park, D.W., Stigler, W.S., Creighton, J., Ravi, S., Darley-Usmar, V., and Zmijewski,
1060 J.W. (2013). Mitochondria and AMP-activated protein kinase-dependent mechanism of
1061 efferocytosis. J Biol Chem *288*, 26013–26026. https://doi.org/10.1074/jbc.M113.489468.

1062 13. Yurdagul, A., Subramanian, M., Wang, X., Crown, S.B., Ilkayeva, O.R., Darville, L., Kolluru,
1063 G.K., Rymond, C.C., Gerlach, B.D., Zheng, Z., et al. (2020). Macrophage Metabolism of
1064 Apoptotic Cell-Derived Arginine Promotes Continual Efferocytosis and Resolution of Injury.
1065 Cell Metab *31*, 518-533.e10. https://doi.org/10.1016/j.cmet.2020.01.001.

1066 14. Merlin, J., Ivanov, S., Dumont, A., Sergushichev, A., Gall, J., Stunault, M., Ayrault, M.,
1067 Vaillant, N., Castiglione, A., Swain, A., et al. (2021). Non-canonical glutamine
1068 transamination sustains efferocytosis by coupling redox buffering to oxidative
1069 phosphorylation. Nat Metab *3*, 1313–1326. https://doi.org/10.1038/s42255-021-00471-y.

1070 15. Tsai, T.-L., Zhou, T.-A., Hsieh, Y.-T., Wang, J.-C., Cheng, H.-K., Huang, C.-H., Tsai, P.-Y.,
1071 Fan, H.-H., Feng, H.-K., Huang, Y.-C., et al. (2022). Multiomics reveal the central role of
1072 pentose phosphate pathway in resident thymic macrophages to cope with efferocytosis-
1073 associated stress. Cell Rep *40*, 111065. https://doi.org/10.1016/j.celrep.2022.111065.

1074 16. He, D., Mao, Q., Jia, J., Wang, Z., Liu, Y., Liu, T., Luo, B., and Zhang, Z. (2021). Pentose
1075 Phosphate Pathway Regulates Tolerogenic Apoptotic Cell Clearance and Immune Tolerance.
1076 Front Immunol *12*, 797091. https://doi.org/10.3389/fimmu.2021.797091.

1077 17. Muckenthaler, M.U., Rivella, S., Hentze, M.W., and Galy, B. (2017). A Red Carpet for Iron
1078 Metabolism. Cell *168*, 344–361. https://doi.org/10.1016/j.cell.2016.12.034.

1079 18. Slusarczyk, P., and Mleczko-Sanecka, K. (2021). The Multiple Facets of Iron Recycling.
1080 Genes (Basel) *12*, 1364. https://doi.org/10.3390/genes12091364.

1081 19. Klei, T.R.L., Meinderts, S.M., van den Berg, T.K., and van Bruggen, R. (2017). From the
1082 Cradle to the Grave: The Role of Macrophages in Erythropoiesis and Erythrophagocytosis.
1083 Front Immunol *8*, 73. https://doi.org/10.3389/fimmu.2017.00073.

1084 20. Kohyama, M., Ise, W., Edelson, B.T., Wilker, P.R., Hildner, K., Mejia, C., Frazier, W.A.,
1085 Murphy, T.L., and Murphy, K.M. (2009). Role for Spi-C in the development of red pulp
1086 macrophages and splenic iron homeostasis. Nature *457*, 318–321.
1087 https://doi.org/10.1038/nature07472.

1088 21. Slusarczyk, P., Mandal, P.K., Zurawska, G., Niklewicz, M., Chouhan, K., Mahadeva, R.,
1089 Jończy, A., Macias, M., Szybinska, A., Cybulska-Lubak, M., et al. (2023). Impaired iron
1090 recycling from erythrocytes is an early hallmark of aging. Elife *12*, e79196.
1091 https://doi.org/10.7554/eLife.79196.

1092 22. Okreglicka, K., Iten, I., Pohlmeier, L., Onder, L., Feng, Q., Kurrer, M., Ludewig, B., Nielsen,
1093 P., Schneider, C., and Kopf, M. (2021). PPARγ is essential for the development of bone
1094 marrow erythroblastic island macrophages and splenic red pulp macrophages. J Exp Med
1095 *218*, e20191314. https://doi.org/10.1084/jem.20191314.

1096 23. Delaby, C., Pilard, N., Puy, H., and Canonne-Hergaux, F. (2008). Sequential regulation of
1097 ferroportin expression after erythrophagocytosis in murine macrophages: early mRNA
1098 induction by haem, followed by iron-dependent protein expression. Biochem J *411*, 123–131.
1099 https://doi.org/10.1042/BJ20071474.

1100 24. Bian, Z., Shi, L., Guo, Y.-L., Lv, Z., Tang, C., Niu, S., Tremblay, A., Venkataramani, M.,
1101 Culpepper, C., Li, L., et al. (2016). Cd47-Sirpα interaction and IL-10 constrain inflammation-
1102 induced macrophage phagocytosis of healthy self-cells. Proc Natl Acad Sci U S A *113*,
1103 E5434-5443. https://doi.org/10.1073/pnas.1521069113.

1104 25. Bennett, L.F., Liao, C., Quickel, M.D., Yeoh, B.S., Vijay-Kumar, M., Hankey-Giblin, P.,
1105 Prabhu, K.S., and Paulson, R.F. (2019). Inflammation induces stress erythropoiesis through
1106 heme-dependent activation of SPI-C. Sci Signal *12*, eaap7336.
1107 https://doi.org/10.1126/scisignal.aap7336.

1108 26. Ma, S., Dubin, A.E., Zhang, Y., Mousavi, S.A.R., Wang, Y., Coombs, A., Loud, M., Andolfo,
1109 I., and Patapoutian, A. (2021). A role of PIEZO1 in iron metabolism in mice and humans.
1110 Cell *184*, 969-982.e13. https://doi.org/10.1016/j.cell.2021.01.024.

1111 27. Camaschella, C. (2019). Iron deficiency. Blood *133*, 30–39. https://doi.org/10.1182/blood-
1112 2018-05-815944.

1113 28. Pasricha, S.-R., Tye-Din, J., Muckenthaler, M.U., and Swinkels, D.W. (2021). Iron
1114 deficiency. Lancet *397*, 233–248. https://doi.org/10.1016/S0140-6736(20)32594-0.

1115 29. GBD 2021 Anaemia Collaborators (2023). Prevalence, years lived with disability, and trends
1116 in anaemia burden by severity and cause, 1990-2021: findings from the Global Burden of
1117 Disease Study 2021. Lancet Haematol *10*, e713–e734. https://doi.org/10.1016/S2352-
1118 3026(23)00160-6.

1119 30. https://www.who.int/publications/m/item/iron-children-6to23--archived-iron-deficiency-
1120 anaemia-assessment-prevention-and-control.

1121 31. Camaschella, C., and Girelli, D. (2020). The changing landscape of iron deficiency. Mol
1122 Aspects Med *75*, 100861. https://doi.org/10.1016/j.mam.2020.100861.

1123 32. Al-Naseem, A., Sallam, A., Choudhury, S., and Thachil, J. (2021). Iron deficiency without
1124 anaemia: a diagnosis that matters. Clin Med (Lond) *21*, 107–113.
1125 https://doi.org/10.7861/clinmed.2020-0582.

1126 33. Prasanth, R. (2017). Prevalence of Anemia in both Developing and Developed Countries
1127 around the World. World Journal of Anemia *1*, 40–43. https://doi.org/10.5005/jp-journals-
1128 10065-0009.

1129 34. Chaparro, C.M., and Suchdev, P.S. (2019). Anemia epidemiology, pathophysiology, and
1130 etiology in low- and middle-income countries. Ann N Y Acad Sci *1450*, 15–31.
1131 https://doi.org/10.1111/nyas.14092.

1132 35. Pasricha, S.-R., Drakesmith, H., Black, J., Hipgrave, D., and Biggs, B.-A. (2013). Control of
1133 iron deficiency anemia in low- and middle-income countries. Blood *121*, 2607–2617.
1134 https://doi.org/10.1182/blood-2012-09-453522.

1135 36. Klei, T.R.L., Dalimot, J., Nota, B., Veldthuis, M., Mul, F.P.J., Rademakers, T.,
1136 Hoogenboezem, M., Nagelkerke, S.Q., van IJcken, W.F.J., Oole, E., et al. (2020). Hemolysis
1137 in the spleen drives erythrocyte turnover. Blood *136*, 1579–1589.
1138 https://doi.org/10.1182/blood.2020005351.

1139 37. Akilesh, H.M., Buechler, M.B., Duggan, J.M., Hahn, W.O., Matta, B., Sun, X., Gessay, G.,
1140 Whalen, E., Mason, M., Presnell, S.R., et al. (2019). Chronic TLR7 and TLR9 signaling
1141 drives anemia via differentiation of specialized hemophagocytes. Science *363*, eaao5213.
1142 https://doi.org/10.1126/science.aao5213.

1143 38. Liu, Z., Gu, Y., Chakarov, S., Bleriot, C., Kwok, I., Chen, X., Shin, A., Huang, W., Dress,
1144 R.J., Dutertre, C.-A., et al. (2019). Fate Mapping via Ms4a3-Expression History Traces
1145 Monocyte-Derived Cells. Cell *178*, 1509-1525.e19.
1146 https://doi.org/10.1016/j.cell.2019.08.009.

1147 39. Palmieri, M., Impey, S., Kang, H., di Ronza, A., Pelz, C., Sardiello, M., and Ballabio, A.
1148 (2011). Characterization of the CLEAR network reveals an integrated control of cellular
1149 clearance pathways. Hum Mol Genet *20*, 3852–3866. https://doi.org/10.1093/hmg/ddr306.

1150 40. Bussi, C., and Gutierrez, M.G. (2024). One size does not fit all: Lysosomes exist in
1151 biochemically and functionally distinct states. PLoS Biol *22*, e3002576.
1152 https://doi.org/10.1371/journal.pbio.3002576.

1153 41. Rovira, M., Sereda, R., Pladevall-Morera, D., Ramponi, V., Marin, I., Maus, M., Madrigal-
1154 Matute, J., Díaz, A., García, F., Muñoz, J., et al. (2022). The lysosomal proteome of senescent

1155 cells contributes to the senescence secretome. Aging Cell *21*, e13707.
1156 https://doi.org/10.1111/acel.13707.

1157 42. Vinchi, F., Costa da Silva, M., Ingoglia, G., Petrillo, S., Brinkman, N., Zuercher, A.,
1158 Cerwenka, A., Tolosano, E., and Muckenthaler, M.U. (2016). Hemopexin therapy reverts
1159 heme-induced proinflammatory phenotypic switching of macrophages in a mouse model of
1160 sickle cell disease. Blood *127*, 473–486. https://doi.org/10.1182/blood-2015-08-663245.

1161 43. Pfefferlé, M., Ingoglia, G., Schaer, C.A., Yalamanoglu, A., Buzzi, R., Dubach, I.L., Tan, G.,
1162 López-Cano, E.Y., Schulthess, N., Hansen, K., et al. (2020). Hemolysis transforms liver
1163 macrophages into antiinflammatory erythrophagocytes. J Clin Invest *130*, 5576–5590.
1164 https://doi.org/10.1172/JCI137282.

1165 44. Pereira, M., Chen, T.-D., Buang, N., Olona, A., Ko, J.-H., Prendecki, M., Costa, A.S.H.,
1166 Nikitopoulou, E., Tronci, L., Pusey, C.D., et al. (2019). Acute Iron Deprivation Reprograms
1167 Human Macrophage Metabolism and Reduces Inflammation In Vivo. Cell Rep *28*, 498-
1168 511.e5. https://doi.org/10.1016/j.celrep.2019.06.039.

1169 45. Pagani, A., Nai, A., Corna, G., Bosurgi, L., Rovere-Querini, P., Camaschella, C., and
1170 Silvestri, L. (2011). Low hepcidin accounts for the proinflammatory status associated with
1171 iron deficiency. Blood *118*, 736–746. https://doi.org/10.1182/blood-2011-02-337212.

1172 46. Diskin, C., and Pålsson-McDermott, E.M. (2018). Metabolic Modulation in Macrophage
1173 Effector Function. Front Immunol *9*, 270. https://doi.org/10.3389/fimmu.2018.00270.

1174 47. Luo, B., Gan, W., Liu, Z., Shen, Z., Wang, J., Shi, R., Liu, Y., Liu, Y., Jiang, M., Zhang, Z., et
1175 al. (2016). Erythropoeitin Signaling in Macrophages Promotes Dying Cell Clearance and
1176 Immune Tolerance. Immunity *44*, 287–302. https://doi.org/10.1016/j.immuni.2016.01.002.

1177 48. Finberg, K.E., Heeney, M.M., Campagna, D.R., Aydinok, Y., Pearson, H.A., Hartman, K.R.,
1178 Mayo, M.M., Samuel, S.M., Strouse, J.J., Markianos, K., et al. (2008). Mutations in
1179 TMPRSS6 cause iron-refractory iron deficiency anemia (IRIDA). Nat Genet *40*, 569–571.
1180 https://doi.org/10.1038/ng.130.

1181 49. Folgueras, A.R., de Lara, F.M., Pendás, A.M., Garabaya, C., Rodríguez, F., Astudillo, A.,
1182 Bernal, T., Cabanillas, R., López-Otín, C., and Velasco, G. (2008). Membrane-bound serine
1183 protease matriptase-2 (Tmprss6) is an essential regulator of iron homeostasis. Blood *112*,
1184 2539–2545. https://doi.org/10.1182/blood-2008-04-149773.

1185 50. Silvestri, L., Pagani, A., Nai, A., De Domenico, I., Kaplan, J., and Camaschella, C. (2008).
1186 The serine protease matriptase-2 (TMPRSS6) inhibits hepcidin activation by cleaving
1187 membrane hemojuvelin. Cell Metab *8*, 502–511. https://doi.org/10.1016/j.cmet.2008.09.012.

1188 51. Meynard, D., Vaja, V., Sun, C.C., Corradini, E., Chen, S., López-Otín, C., Grgurevic, L.,
1189 Hong, C.C., Stirnberg, M., Gütschow, M., et al. (2011). Regulation of TMPRSS6 by BMP6
1190 and iron in human cells and mice. Blood *118*, 747–756. https://doi.org/10.1182/blood-2011-
1191 04-348698.

1192 52. Sawyer, D.W., Sullivan, J.A., and Mandell, G.L. (1985). Intracellular free calcium
1193 localization in neutrophils during phagocytosis. Science *230*, 663–666.
1194 https://doi.org/10.1126/science.4048951.

1195 53. Shen, J., Wilbon, A.S., Zhou, M., and Pan, Y. (2023). Mechanism of Ca2+ transport by
1196 ferroportin. Elife *12*, e82947. https://doi.org/10.7554/eLife.82947.

1197 54. Zumerle, S., Calì, B., Munari, F., Angioni, R., Di Virgilio, F., Molon, B., and Viola, A.
1198 (2019). Intercellular Calcium Signaling Induced by ATP Potentiates Macrophage
1199 Phagocytosis. Cell Rep *27*, 1-10.e4. https://doi.org/10.1016/j.celrep.2019.03.011.

1200 55. Beard, J. (2003). Iron deficiency alters brain development and functioning. J Nutr *133*,
1201 1468S-72S. https://doi.org/10.1093/jn/133.5.1468S.

1202 56. Badaracco, M.E., Ortiz, E.H., Soto, E.F., Connor, J., and Pasquini, J.M. (2008). Effect of
1203 transferrin on hypomyelination induced by iron deficiency. J Neurosci Res *86*, 2663–2673.
1204 https://doi.org/10.1002/jnr.21709.

1205 57. Jiang, Y., Li, C., Wu, Q., An, P., Huang, L., Wang, J., Chen, C., Chen, X., Zhang, F., Ma, L.,
1206 et al. (2019). Iron-dependent histone 3 lysine 9 demethylation controls B cell proliferation
1207 and humoral immune responses. Nat Commun *10*, 2935. https://doi.org/10.1038/s41467-019-
1208 11002-5.

1209 58. Zhu, L., Li, G., Liang, Z., Qi, T., Deng, K., Yu, J., Peng, Y., Zheng, J., Song, Y., and Chang,
1210 X. (2023). Microbiota-assisted iron uptake promotes immune tolerance in the intestine. Nat
1211 Commun *14*, 2790. https://doi.org/10.1038/s41467-023-38444-2.

1212 59. Wang, L., Johnson, E.E., Shi, H.N., Allan Walker, W., Wessling-Resnick, M., and Cherayil,
1213 B.J. (2008). Attenuated inflammatory responses in hemochromatosis reveal a role for iron in
1214 the regulation of macrophage cytokine translation. J Immunol *181*, 2723–2731.

1215 60. Agoro, R., Taleb, M., Quesniaux, V.F.J., and Mura, C. (2018). Cell iron status influences
1216 macrophage polarization. PLoS One *13*, e0196921.
1217 https://doi.org/10.1371/journal.pone.0196921.

1218 61. Mleczko-Sanecka, K., and Silvestri, L. (2021). Cell-type-specific insights into iron regulatory
1219 processes. Am J Hematol *96*, 110–127. https://doi.org/10.1002/ajh.26001.

1220 62. Xu, W., Barrientos, T., Mao, L., Rockman, H.A., Sauve, A.A., and Andrews, N.C. (2015).
1221 Lethal Cardiomyopathy in Mice Lacking Transferrin Receptor in the Heart. Cell Rep *13*,
1222 533–545. https://doi.org/10.1016/j.celrep.2015.09.023.

1223 63. Banerjee, S., Lu, S., Jain, A., Wang, I., Tao, H., Srinivasan, S., Nemeth, E., and He, P. (2024).
1224 Targeting PKCa alleviates iron overload in diabetes and hemochromatosis through the
1225 inhibition of ferroportin. Blood, blood.2024023829.
1226 https://doi.org/10.1182/blood.2024023829.

1227 64. Ennerfelt, H., Frost, E.L., Shapiro, D.A., Holliday, C., Zengeler, K.E., Voithofer, G., Bolte,
1228 A.C., Lammert, C.R., Kulas, J.A., Ulland, T.K., et al. (2022). SYK coordinates
1229 neuroprotective microglial responses in neurodegenerative disease. Cell *185*, 4135-4152.e22.
1230 https://doi.org/10.1016/j.cell.2022.09.030.

1231 65. Wang, S., Sudan, R., Peng, V., Zhou, Y., Du, S., Yuede, C.M., Lei, T., Hou, J., Cai, Z., Cella,
1232 M., et al. (2022). TREM2 drives microglia response to amyloid-β via SYK-dependent and -
1233 independent pathways. Cell *185*, 4153-4169.e19. https://doi.org/10.1016/j.cell.2022.09.033.

1234 66. Kobayashi, A., Azuma, K., Takeiwa, T., Kitami, T., Horie, K., Ikeda, K., and Inoue, S. (2023).
1235 A FRET-based respirasome assembly screen identifies spleen tyrosine kinase as a target to
1236 improve muscle mitochondrial respiration and exercise performance in mice. Nat Commun
1237 *14*, 312. https://doi.org/10.1038/s41467-023-35865-x.

1238 67. Canton, J., Khezri, R., Glogauer, M., and Grinstein, S. (2014). Contrasting phagosome pH
1239 regulation and maturation in human M1 and M2 macrophages. Mol Biol Cell *25*, 3330–3341.
1240 https://doi.org/10.1091/mbc.E14-05-0967.

1241 68. Das Gupta, K., Shakespear, M.R., Curson, J.E.B., Murthy, A.M.V., Iyer, A., Hodson, M.P.,
1242 Ramnath, D., Tillu, V.A., von Pein, J.B., Reid, R.C., et al. (2020). Class IIa Histone
1243 Deacetylases Drive Toll-like Receptor-Inducible Glycolysis and Macrophage Inflammatory
1244 Responses via Pyruvate Kinase M2. Cell Rep *30*, 2712-2728.e8.
1245 https://doi.org/10.1016/j.celrep.2020.02.007.

1246 69. Codo, A.C., Davanzo, G.G., Monteiro, L. de B., de Souza, G.F., Muraro, S.P., Virgilio-da-
1247 Silva, J.V., Prodonoff, J.S., Carregari, V.C., de Biagi Junior, C.A.O., Crunfli, F., et al. (2020).
1248 Elevated Glucose Levels Favor SARS-CoV-2 Infection and Monocyte Response through a
1249 HIF-1α/Glycolysis-Dependent Axis. Cell Metab *32*, 437-446.e5.
1250 https://doi.org/10.1016/j.cmet.2020.07.007.

1251 70. Van den Bossche, J., O'Neill, L.A., and Menon, D. (2017). Macrophage Immunometabolism:
1252 Where Are We (Going)? Trends Immunol *38*, 395–406.
1253 https://doi.org/10.1016/j.it.2017.03.001.

1254 71. Divakaruni, A.S., Hsieh, W.Y., Minarrieta, L., Duong, T.N., Kim, K.K.O., Desousa, B.R.,
1255 Andreyev, A.Y., Bowman, C.E., Caradonna, K., Dranka, B.P., et al. (2018). Etomoxir Inhibits
1256 Macrophage Polarization by Disrupting CoA Homeostasis. Cell Metab *28*, 490-503.e7.
1257 https://doi.org/10.1016/j.cmet.2018.06.001.

1258 72. Liu, P.-S., Wang, H., Li, X., Chao, T., Teav, T., Christen, S., Di Conza, G., Cheng, W.-C.,
1259 Chou, C.-H., Vavakova, M., et al. (2017). α-ketoglutarate orchestrates macrophage activation
1260 through metabolic and epigenetic reprogramming. Nat Immunol *18*, 985–994.
1261 https://doi.org/10.1038/ni.3796.

1262 73. Mills, E.L., Kelly, B., Logan, A., Costa, A.S.H., Varma, M., Bryant, C.E., Tourlomousis, P.,
1263 Däbritz, J.H.M., Gottlieb, E., Latorre, I., et al. (2016). Succinate Dehydrogenase Supports
1264 Metabolic Repurposing of Mitochondria to Drive Inflammatory Macrophages. Cell *167*, 457-
1265 470.e13. https://doi.org/10.1016/j.cell.2016.08.064.

1266 74. Torrance, J.D., and Bothwell, T.H. (1968). A simple technique for measuring storage iron
1267 concentrations in formalinised liver samples. S Afr J Med Sci *33*, 9–11.

1268 75. Moggridge, S., Sorensen, P.H., Morin, G.B., and Hughes, C.S. (2018). Extending the
1269 Compatibility of the SP3 Paramagnetic Bead Processing Approach for Proteomics. J
1270 Proteome Res *17*, 1730–1740. https://doi.org/10.1021/acs.jproteome.7b00913.

1271 76. Hughes, C.S., Foehr, S., Garfield, D.A., Furlong, E.E., Steinmetz, L.M., and Krijgsveld, J.
1272 (2014). Ultrasensitive proteome analysis using paramagnetic bead technology. Mol Syst Biol
1273 *10*, 757. https://doi.org/10.15252/msb.20145625.

1274 77. Werner, T., Sweetman, G., Savitski, M.F., Mathieson, T., Bantscheff, M., and Savitski, M.M.
1275 (2014). Ion coalescence of neutron encoded TMT 10-plex reporter ions. Anal Chem *86*,
1276 3594–3601. https://doi.org/10.1021/ac500140s.

1277 78. Yang, F., Shen, Y., Camp, D.G., and Smith, R.D. (2012). High-pH reversed-phase
1278 chromatography with fraction concatenation for 2D proteomic analysis. Expert Rev
1279 Proteomics *9*, 129–134. https://doi.org/10.1586/epr.12.15.

1280